DAO Office Note 2001-11

Office Note Series on Global Modeling and Data Assimilation

One-dimensional Variational Analysis using GPS radio occultation refractivity

Paul Poli[1,2]
Joanna Joiner[3]
Emil Robert Kursinski[4,5]

Data Assimilation Office, Goddard Laboratory for Atmospheres
[1] *Joint Center for Earth Systems Technology, Baltimore, Maryland*
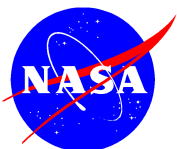[2] *Météo France Centre National de Recherches Météorologiques, Toulouse, France*
[3] *Laboratory for Atmospheres, Greenbelt, Maryland*
[4] *Jet Propulsion Laboratory, Pasadena, California*
[5] *University of Arizona, Tucson, Arizona*

Goddard Space Flight Center
Greenbelt, Maryland 20771
November 2001

Abstract

The Global Positioning System (GPS) employs a constellation of satellites which provides a stable source of electromagnetic signals available for radio occultation purposes about our planet. The atmospheric-induced bending of the transmitted rays can be converted into a refractivity profile for each occultation using an Abel transform. Since refractivity is related to temperature and humidity, it may be used for global data assimilation into climate and/or Numerical Weather Prediction (NWP) models. We implement here a low computing cost one-dimensional variational (1DVAR) analysis of GPS refractivity which enables retrieving temperature, humidity and sea level pressure. To assess the potential information content of the measurements, we perform a linear error analysis and fully non-linear Monte-Carlo simulations. They show the potential impact of the GPS to improve upon an accurate background from a Data Assimilation System (DAS). 1DVAR retrievals based on data collected during the GPS/MET 1995 experiment are compared with collocated radiosondes. They show an excellent capacity of the GPS measurements to resolve the tropopause. In the northern hemisphere, we demonstrate a net reduction of temperature bias and standard deviation, as compared with the Goddard Earth Observing System (GEOS) DAS and the Finite Volume DAS (FVDAS) backgrounds. We point out significant sensitivities of the retrievals to the gravitational constant, the number of analysis levels, the surface pressure and the background and observation assumed errors. We relate the analysis of refractivity to the 1DVAR increments (analysis minus background). This represents a step towards using the GPS data in data assimilation systems to improve NWP forecasts and representation of Earth's climate.

Contents

List of Figures

List of Tables

1   Introduction

The Global Positioning System (GPS) system provides continuous radio signals for precise positioning in the immediate vicinity of our planet. The atmosphere affects the speed of propagation of these signals. These perturbations in the GPS signals can in turn be used to remotely sense the atmosphere. In particular, by placing a receiver in Low Earth Orbit (LEO, e.g. 500 to 2000 km altitude) it is possible to perform soundings using the limb-viewing radio occultation (RO) technique. Radio occultation has been used for more than thirty years to study the atmospheres of other planets [e.g. *Fjeldbo et al.*, 1971; *Lindal et al.*, 1979, 1981; *Tyler et al.*, 1982; *Lindal*, 1992; *Jenkins et al.*, 1994]. *Gorbunov and Sokolovskiy* [1993] provided simulations of GPS radio occultation measurements. *Kursinski et al.* [1997] also simulated many aspects of GPS measurements and their expected error characteristics. GPS/MET (1995) was the first radio occultation experiment conducted on Earth using radio occultation [e.g. *Kursinski et al.*, 1996, *Ware et al.*, 1996].

Before using the GPS data in a data assimilation system for numerical weather prediction (NWP) or climate study, a first step is to appraise the impact these data have on the analysis. One technique for assessing impact is the Observing System Simulation Experiment (OSSE). *Kuo et al.* [1997] have performed OSSE's with simulated GPS data. There are known limitations of OSSE's [e.g. *Atlas*, 1997] and therefore care must be taken when interpreting the results. For example, no observation errors were included in the *Kuo et al.* [1997] OSSE. We will give an example of the effect of neglecting errors in a simulation.

In this work, both simulated and real observations are analyzed to gauge the impact of GPS data on an analysis. For this purpose, we have developed a one dimensional variational (1DVAR) analysis of temperature, humidity and sea level pressure. In this approach, background information from a General Circulation Model (GCM) forecast is used to constrain the retrievals. Based on the assumed observation and background errors, the approach also yields an estimate of the analysis errors.

The outline of the paper is as follows : First we give a brief description of the GPS radio occultation technique and discuss the different possible approaches to retrieve and assimilate atmospheric properties from GPS measurements. Then, we describe the implementation of a 1DVAR analysis of refractivity. After this, we show results of Monte-Carlo simulations and linear error analysis. We then discuss sensitivities of the GPS analyses to various parameters, and compare GPS/MET 1DVAR retrievals with nearby radiosondes. Finally, we attempt to interpret the 1DVAR analyses in the light of the refractivity differences between the background and the observations.

2   The Global Positioning System

The GPS was designed by the U.S. Department of Defense (USDoD). Its main purpose is to aid in navigation. It enables accurate positioning anywhere about the globe. It consists of 24 orbiting satellites distributed in six orbital planes. The 20,200 km altitude orbits are circular with an inclination of $55°$ and a period of 12 hours. The principle of the GPS is based on the path delay of a propagating radio signal. Two L-band frequencies are used : L_1 1575.42 MHz (or 19.0 cm) and L_2 1227.60 MHz (or

24.4 cm).

The accuracy of GPS measurements is intentionally degraded by encryption for security reasons. This is known as "Anti-Spoofing". First-generation receivers were launched on GPS/MET (1995). Their ability to track the occultations is degraded when the encryption is on, which is generally the case except during very short periods for scientific studies. Second-generation GPS receivers built for the purposes of the radio occultation are to be flown on the missions Champ (Germany) and SAC-C (Argentina). These receivers are able to better process encoded signals, for which the L_2 signal-to-noise (SNR) ratio is very low.

The accuracy of positioning is limited by several factors [e.g. *Doerflinger*, 1998]. First, the exact position and velocity of the GPS satellites must be known perfectly (at a given time) to position a receiver relative to them. It follows that (1) orbit errors (2) clock drifts (3) relativistic effects (4) receiver system errors (antenna and receiver noise) and (5) use of approximate co-ordinates contribute to the total error of the measurement. Other perturbations in signals that degrade the quality of the positioning for a terrestrial receiver are caused by atmospheric refraction and scattering which may cause multipath effects.

The applications of GPS to meteorology include positioning *in situ* measurements [*Hein et al.*, 1990], computing wind speed from the drift of radiosondes [*Saarnimo*, 1998], and measuring the total column of water vapor above a ground-based receiver [e.g. *Bevis et al.*, 1992, *Elgered et al.*, 1997]. In this study, we focus on space-based GPS receivers.

3   Radio Occultation with GPS

We remind here briefly the advantages and concepts associated with the GPS radio occultation technique.

3.1   Features of the GPS Radio Occultation Technique

There are several interesting attributes of GPS occultations as an atmospheric sounding device. A high-inclination LEO provides a set of observations that covers the globe fairly uniformly at a relatively low cost [*Yunck et al.*, 1988]. The homogeneity of the GPS coverage is advantageous for providing global observations in comparison to balloon-launched radiosondes (about 800 each 12 hours, the majority of which are over the northern hemisphere continents). A single GPS receiver can obtain approximately 500 occultations per day [*Kursinski et al.*, 1997]. This number per GPS receiver is less than the number of profiles obtained by a sounder on-board a meteorological polar-orbiting satellite. In order to collect more occultations per day, one must place more receivers into orbit, which is feasible because the receivers are simple and small.

When compared within Infra-Red (IR) spaceborne sounders, the radio occultation (RO) technique with GPS has the advantage of being an "all-weather" system. Like Micro-Wave (MW) and unlike IR sounders, it is scarcely sensitive to aerosols and

clouds. In addition, it is also insensitive to rain due to wavelengths of order 20 cm. Unlike most other techniques the GPS radio occultation provides a degree of self-calibration, because relative phase shifts are the relevant information. Moreover, the stability of the transmitter and receiver clocks limits temporal drifts.

Finally, due to its limb-viewing geometry and Fresnel diffraction, the GPS RO has a higher vertical resolution (0.2-1.5 km) than passive nadir sounders [*Kursinski et al.*, 1997]. This vertical resolution is more comparable to radiosondes. Furthermore, the ratio between vertical and horizontal resolution (about 300 km) is consistent with that of quasi-geostrophic flows [*Lindzen and Fox-Rabinovitz*, 1989; *Kursinski et al.*, 1997].

3.2 Configuration of a GPS Occultation

Multiple GPS transmitters are tracked continuously to determine position and velocity. One transmitter is used for clock correction. Another transmitter is used for the occultation. The rays from the source (occulted transmitter) traverse the Earth's atmospheric limb to reach the receiver.

Whenever an electromagnetic signal passes through the atmosphere, it is refracted according to Snell's law, due to the vertical gradient of refractivity. As compared with what would happen in a vacuum, (1) the bending lengthens the ray path and (2) the waves travel slower because the refractive index is not unity. Also, the signal is affected by atmospheric absorption and scattering. For L-band (large) wavelengths, the scattering effect may be neglected with realistic liquid water and ice contents [*Kursinski et al.*, 1995].

Since the two satellites are in relative motion, the refraction introduces a change in the Doppler shift of the received signal. After removal of the phase change due to the relative motion of the LEO with respect to the GPS, proper calibration of receiver and transmitter clocks, the extra phase change induced by the atmosphere can be isolated.

The overall effect of the atmosphere can be summed up by a total bending angle ε and an asymptotic ray-miss distance p (commonly called impact parameter) as shown in figure 1. The distance between the perigee point and the center of curvature is r_t. The vertical scanning of the atmosphere is provided by the relative motion between the two orbiting satellites as depicted in figure 2. Time dependency of both ε and p can be derived from accurate measurements of Doppler-shifted frequency.

3.3 Inversion of Bending Angles to Refractivity

The bending induced by the atmosphere ranges approximately between $(2 \times 10^{-5})°$ at 80 km altitude and $1°$ nearby the surface [*Kursinski et al.*, 1997]. The horizontal path covered by this bending is about 1.5 km wide and 200-300 km long, centered on the tangent point (see figure 3). A typical occultation lasts between 1 and 2 minutes.

The variation of refractive index n along a limb path in the Earth's atmosphere is dominated by the vertical gradient. To the first order, the refractive index field is
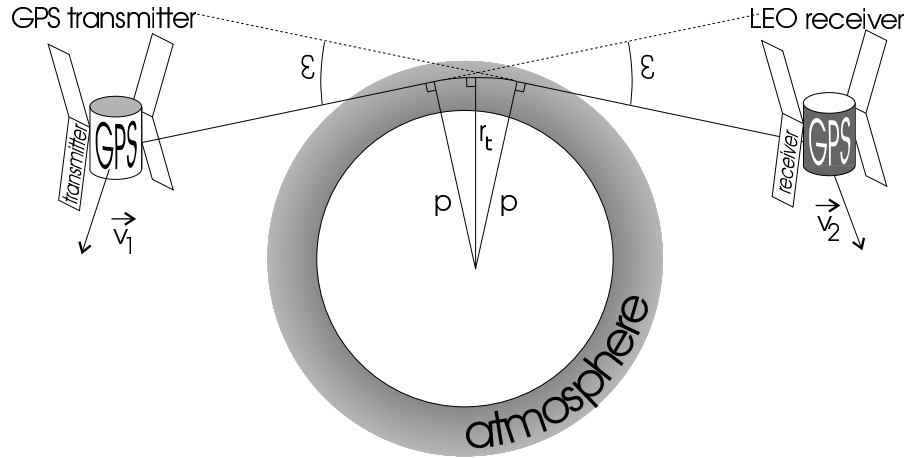
Figure 1: Geometry of a GPS occultation under the hypothesis of spherical symmetry of the atmosphere.
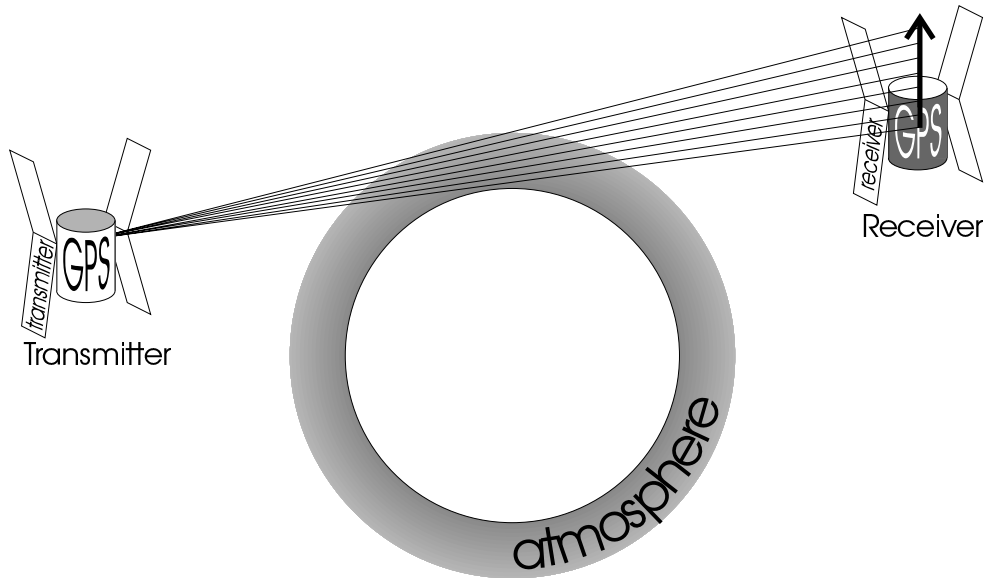
Figure 2: Vertical scanning of the atmosphere during an occultation.
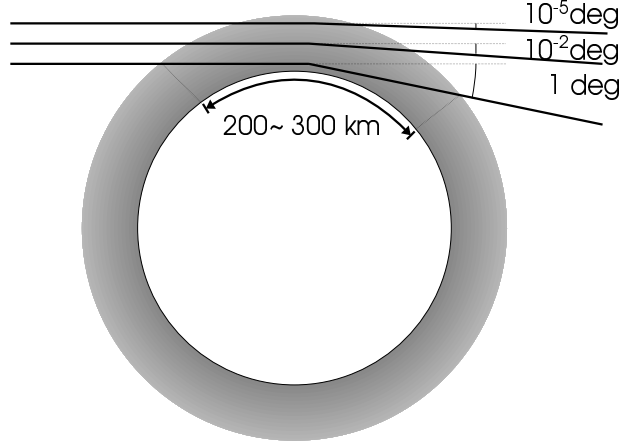
Figure 3: Bending of the rays during an occultation.

spherically symmetric. If p is the impact parameter for the tangent ray whose radius is r, the bending angle ε can be expressed by :

$$\varepsilon\left(p\right) = -2p \int_{p}^{\infty} \left(\frac{\partial \ln n}{\partial x}\right) \left(x^2 - p^2\right)^{-\frac{1}{2}} dx, \tag{1}$$

where $x = rn$ [e.g. *Fjeldbo et al., 1971*]. An elegant and direct way to obtain n from ε and p is to use Abelian transformation assuming a local spherical symmetry, i.e. :

$$n\left(x\right) = \exp\left[\frac{1}{\pi} \int_{x}^{\infty} \varepsilon\left(p\right) \left(p^2 - x^2\right)^{-\frac{1}{2}} dp\right], \tag{2}$$

[e.g. *Fjeldbo et al., 1971*].

Errors in computing n by this approach result from [*Kursinski et al., 1997*] (1) local spherical asymmetry [*Ahmad and Tyler, 1999*], (2) non-coplanar rays, (3) non-vertical scanning (because both satellites drift during an occultation [*Eyre, 1994*]) and (4) an inaccurate upper boundary used to initiate the integral [*Steiner et al., 1999*]. The integral formulation of the Abel transform spreads the errors in this boundary condition along the vertical.

3.4   Interpretation of Refractivity

For microwave frequencies, the refractivity N (defined by $N = 10^6 \left(n - 1\right)$) of the atmosphere can be expressed by :

$$N = b_1 \frac{P}{T} + b_2 \frac{P_w}{T^2} + b_3 \frac{N_e}{f^2} + b_4 W, \tag{3}$$

5

[e.g. *Kursinski et al.,* 1997] where f is the frequency of the signal emitted by the transmitter in Hz, P the pressure of air (dry air and water vapor) in hPa, T the temperature in K, P_w the partial pressure in water vapor in hPa, N_e the electrons density in m^{-3}, and W the particulates density (primarily liquid water) in $g \cdot m^{-3}$. The b_i are constants; $b_1 = 77.6$ N-unit$\cdot$K$\cdot$hPa^{-1}, $b_2 = 3.73 \times 10^5$ N-unit$\cdot$K$^2\cdot$hPa^{-1}, $b_3 = 40.3 \times 10^6$ N-unit$\cdot$Hz$^2\cdot$m^3, $b_4 = 1.4$ N-unit$\cdot$g$^{-1}\cdot$m^3.

The four refractivity terms in equation 3 are often referred to as (1) hydrostatic (or dry), (2) moist, (3) ionospheric and (4) scattering terms, respectively. The first term is due to the polarizability of atmospheric molecules. It is dominant below 60-90 km. The second term is due to the fact that the water molecule is polar. The ionospheric term results from the free electrons of the ionosphere. It can be removed by the use of the two GPS frequencies f_1 and f_2 [*Vorob'ev and Krasil'nikova,* 1994]. The last term can be neglected, as explained in section 3.2. Therefore, after removing the ionospheric component, N can be approximated by [e.g. *Bean and Dutton,* 1966] :

$$N = b_1 \frac{P}{T} + b_2 \frac{P_w}{T^2}. \tag{4}$$

4   Use of GPS for Atmospheric Retrievals and Data Assimilation

There are commonly three levels of GPS radio occultation data available for data assimilation [*Zou et al.,* 1999]: (1) bending angles, (2) refractivity and (3) retrieved profiles of temperature or water vapor. To be assimilated, each level requires an estimate of the errors and an observation operator along with its tangent linear model (TLM) or adjoint [*Eyre et al.,* 1993]. The observation operator converts model conventional variables (i.e. temperature, humidity, pressure) into observed GPS data such as bending angles or refractivity.

4.1   Assimilation of Bending Angles

These are considered as the "rawest" data (even though Doppler shifts themselves represent an even rawer form of the data). An estimate of the error in each refracted angle measurement is needed. One advantage of using these data is that the observation errors are relatively uncorrelated with respect to each other. Also, the number of processing steps necessary to obtain these data is the smallest. Hence they should provide the highest accuracy.

However, the observation operator is quite complex [*Eyre,* 1994]. First, it has to interpolate the background information (typically gridded fields from a numerical weather prediction model) for temperature, humidity and pressure to each measurement location. This requirement stands for all approaches. Second, it has to compute the refracted angle ε and its tangent linear model for a given value of an impact parameter p. This implies computing the derivative of the local refractivity at each point, which is subject to high variability.

Full ray-tracing codes have been developed by *Mortensen and Høeg* [1998] and *Zou*

et al. [1999]. They have the capability to reconstruct the ray path and simulate the overall bending angle from a given state of atmosphere. However, assimilating 30 profiles with a ray-tracing model in the National Centers for Environmental Prediction Data Assimilation System (NCEP-DAS) requires approximately 4 hours of CPU (Central Processing Unit) on a Cray C-90 computer [*Matsumura et al.*, 1999]. Currently, the ray-tracing approach is likely to be too expensive for operational data assimilation.

Another approach for the observation operator consists of assuming spherical symmetry. Such one-dimensional operators have been developed by *Healy* [1998], *Palmer* [1998], and *Zuffada et al.* [1999]. Like the 3D approach, it still involves local derivatives of refractivity, but the computational cost is significantly lower than a full ray-tracing.

4.2 Assimilation of Retrieved Profiles of Refractivity

In this approach, the bending angles have to first be inverted with an Abel transform to obtain profiles of refractivity as a function of altitude. The observation operator calculates refractivity from interpolated model variables using (4). This is much simpler and less computationally burdensome than simulating bending angles.

The drawback to this approach is that additional errors are introduced by the Abel transform as described in section 3.3. The vertical correlation in these errors must be accounted for to achieve accurate assimilation.

4.3 Assimilation of Retrieved Profiles of Temperature and/or Humidity

Using the refractivity information, temperature and/or humidity can be retrieved [*Kursinski et al.*, 1995]. The retrieval error can be separated into three components [*Rodgers*, 1990] : (1) random error due to measurement noise (2) systematic error due to uncertain model parameters and inversion model bias (3) null-space error due to the inherent finite vertical resolution of the observing system (this is actually the background error component). The *main point* is that temperature and humidity errors in the retrievals are correlated both vertically and horizontally. These errors are difficult to estimate.

The simplicity of assimilating retrieved profiles of temperature and/or humidity is that the data are essentially the same as those used in a NWP model. Therefore, the observation operator is trivial.

4.4 Summary on the Various Approaches

Bending angles have the simplest error but the most complicated and expensive observation operator. Conversely, retrieved temperature or humidity profiles have the

simplest observation operator, but the most complicated errors. The errors accumulate all the approximations made during the conversion of raw GPS data into meteorological values. Assimilating refractivity represents a good alternative with a relatively low computing cost.

The approach chosen here is to retrieve both temperature and humidity in a one-dimensional (1D, over the vertical) 'off-line' analysis based on a model forecast first guess and refractivity measurements.

5   GPS-1DVAR Implementation

We describe now the one-dimensional variational (1DVAR) analysis scheme and its components in detail.

5.1   Variational Theory

The application of variational analysis to the retrieval of geophysical parameters has been discussed extensively by several authors [e.g. *Rodgers*, 1976; *Eyre at al.*, 1993]. We try to minimize a cost function $\mathcal{J}$ with respect to a variable state of atmosphere x (state vector). This function is

$$\mathcal{J}[x] = (h(x) - y^0)^T (O + F)^{-1} (h(x) - y^0) + (x - x^b)^T B^{-1} (x - x^b), \qquad (5)$$

[e.g. *Jazwinski*, 1970] where y^0 is the observation vector, h is the observation operator (non-linear), x^b is the background information (for example a 6-hour forecast), O, B, and F are the error covariance matrices of the observations, observation operator, and background, respectively. Hence $h(x)$ is an estimate of the observations that would be made with a state of the atmosphere x.

The minimum variance problem can be solved using a quasi-Newton iteration, *i.e.*,

$$x_{i+1} = x^b + \left(H_i^T R^{-1} H_i + B^{-1} \right)^{-1} H_i^T R^{-1} \left(y^0 - h(x) + H_i \left(x_i - x^b \right) \right), \qquad (6)$$

[e.g. *Rodgers*, 1976] where the subscript i denotes the iteration number, $R = O + F$, H_i is the tangent linear model of the observation operator h, or Jacobian, and H_i^T the adjoint. We define convergence as the iteration at which the quantity $\mathcal{J}[x_i]$ has changed by less than 2% from the previous iteration, because further iterations did not make appreciable changes in the analysis. *Healy and Eyre* [2000] and *Palmer et al.* [2000] have found that the cost function at convergence can be used to quality control the GPS observations.

After convergence, (6) represents a solution (the *analysis*) that has an optimal position or distance with respect to both the observations and the background provided that the background and observation errors are unbiased, normally distributed, and uncorrelated with respect to each other. Since these three postulates may not always be true, we obtain a sub-optimal solution. A bias estimate is one way to address one aspect of the problem [*Dee and da Silva*, 1998].

5.2 The State Vector

Our state vector includes the temperature, the negative of the log of the specific humidity at the background pressure levels, and the sea level pressure. Since GPS has virtually no sensitivity to humidity less than 0.1 g/kg [*Kursinski and Hajj,* 2000], the humidity is removed from the state vector above a specified level (50 hPa).

In the implementation, the state vector extends only to the lowest perigee point of the occultation. If n_T is the number of temperature levels, n_{P_w} the number of background levels with water vapor in the state variable, the state vector x contains $(n_T + n_{P_w} + 1)$ elements :

$$x = \left(T_1, T_2, \ldots, T_{n_T}, -\log q_1, -\log q_2, \ldots, -\log q_{n_{P_w}}, P_{sea\ level} \right). \qquad (7)$$

5.3 Background Information

We used four different types of background for our analysis. The first two date back from 1995, and the two others date from 2000.

5.3.1 GEOS Background: forecast and assimilation

We first used background information from the Goddard Earth Observing System (GEOS) Data Assimilation System (DAS) version 1 for our analysis. It included upper stratospheric levels (GEOS-Strat). Since the 6-hour forecast [*Takacs et al.,* 1994; *Schubert et al.,* 1995] was only archived on 18 selected pressure levels (surface up to 0.4 hPa), we used a second set of background information, a product called the 'assimilation', available on the 46 σ levels of the General Circulation Model (GCM) from the surface up to 0.1 hPa.

The Data Assimilation Office (DAO) GEOS-DAS version 1 uses an Incremental Analysis Update (IAU) approach [*Bloom et al.,* 1996] in an Optimal Interpolation (OI) framework [*Pfaendtner et al.,* 1995]. It consists of applying gradual analysis increments to the model integration within the 6-hour assimilation window. The 'assimilation' is the result of this operation in the middle of the window. So this second set of background information already contained some information from the observations available during the assimilation period (especially radiosondes).

In the rest of the paper, we will subsequently refer to these two backgrounds as 'GEOS Forecast' (18 levels), and 'GEOS Assimilation' (46 levels).

5.3.2 FVDAS Background: NESDIS TOVS and DAOTOVS forecasts

Since the previous background information showed obvious discrepancies when comparing with radiosondes, especially temperature biases at the tropopause (see later), we decided to use a state-of-the-art background. The Finite-Volume DAS (FVDAS)

[*DAO*, 2000] combines a Physical-space Statistical Analysis System (PSAS) assimilation scheme [*Cohn et al.*, 1998] and a NASA/NCAR (National Aeronautics and Space Administration/National Center for Atmospheric Research) GCM. One significant feature of the FVDAS resides in the dynamical core of the GCM which uses a Lagrangian vertical coordinate system [*Lin*, 1997]. As will be seen later, the improvements between the GEOS and the FVDAS systems are obvious in terms of temperature when comparing with radiosondes. To initialize the model we used Atmospheric Model Inter-comparison Project (AMIP) climatological 'cold' runs, and then did a spin-up of three weeks by assimilation of the observations (mainly RS and TOVS) from June 1st 1995 until the June 21st-July 4th 1995 period.

One important source of observations for the DAS comes from the TIROS Operational Vertical Sounder (TOVS) soundings. The National Oceanic and Atmospheric Administration (NOAA) National Environmental Satellite, Data, and Information Service (NESDIS) provides operationally profiles of retrieved temperature and humidity. These profiles are obtained *via* a complex retrieval method which does not involve short-term GCM forecast [*Reale et al.*, 1994]. Another source of TOVS observations is the DAOTOVS system, which relies on a variational cloud-clearing embedded in the assimilation cycle. It uses the latest available 6-hour forecast as a background to initiate the retrievals and includes a Kalman-filtered bias correction based on radiosondes [*Joiner and Rokke*, 2000]. Considering the very different results obtained using either NESDIS TOVS or DAOTOVS as observation sources, we chose to include both backgrounds in the present paper in order to show that the impact of GPS refractivity data on an analysis can change depending on the quality of the background, and of the other data types (independent of GPS) which are assimilated.

In the rest of the paper, we will subsequently refer to these two 6-hour forecasts backgrounds as 'FVDAS NESDIS TOVS' and 'FVDAS DAOTOVS'. Both are specified on the same 46 σ levels as the GEOS Assimilation.

5.3.3 Background error covariance matrix

The same background error covariance matrix is used in the four sets of backgrounds. It uses variances from *Joiner and Rokke* [2000]. For temperature, it includes inter-level correlations through the following formula :

$$Cov(T_i, T_j) = \sigma_{T_i} \sigma_{T_j} \exp\left(-(\frac{\log(P_i/P_j)}{\Delta L})^2\right) \exp\left(-(\frac{T_i - Tj}{\Delta T})^2\right), \qquad (8)$$

where $Cov(T_i, T_j)$ expresses the temperature error covariance between two levels i and j, σ_{T_i} is the temperature error standard deviation for the pressure level P_i, T_i is the temperature at that level, $\Delta L = 0.1$, and $\Delta T = 3$ are constants which were experimentally adjusted. Using this formulation, two levels close in log of pressure and temperature have highly-correlated errors. In order to take into account the variable altitude of the tropopause, we added a feature to the scheme to fit the local maximum of model error to the altitude of the minimum of temperature. Figure 4 shows the diagonal of the background error covariance matrix for temperature.

We follow here a conservative approach to estimate the impact of the GPS data on the quality of a 1DVAR analysis. Therefore, we assume relatively small background errors, i.e. that the background accuracy will be of the order of 1K. While these values

ADAPTATION OF THE B MATRIX TO THE TROPOPAUSE
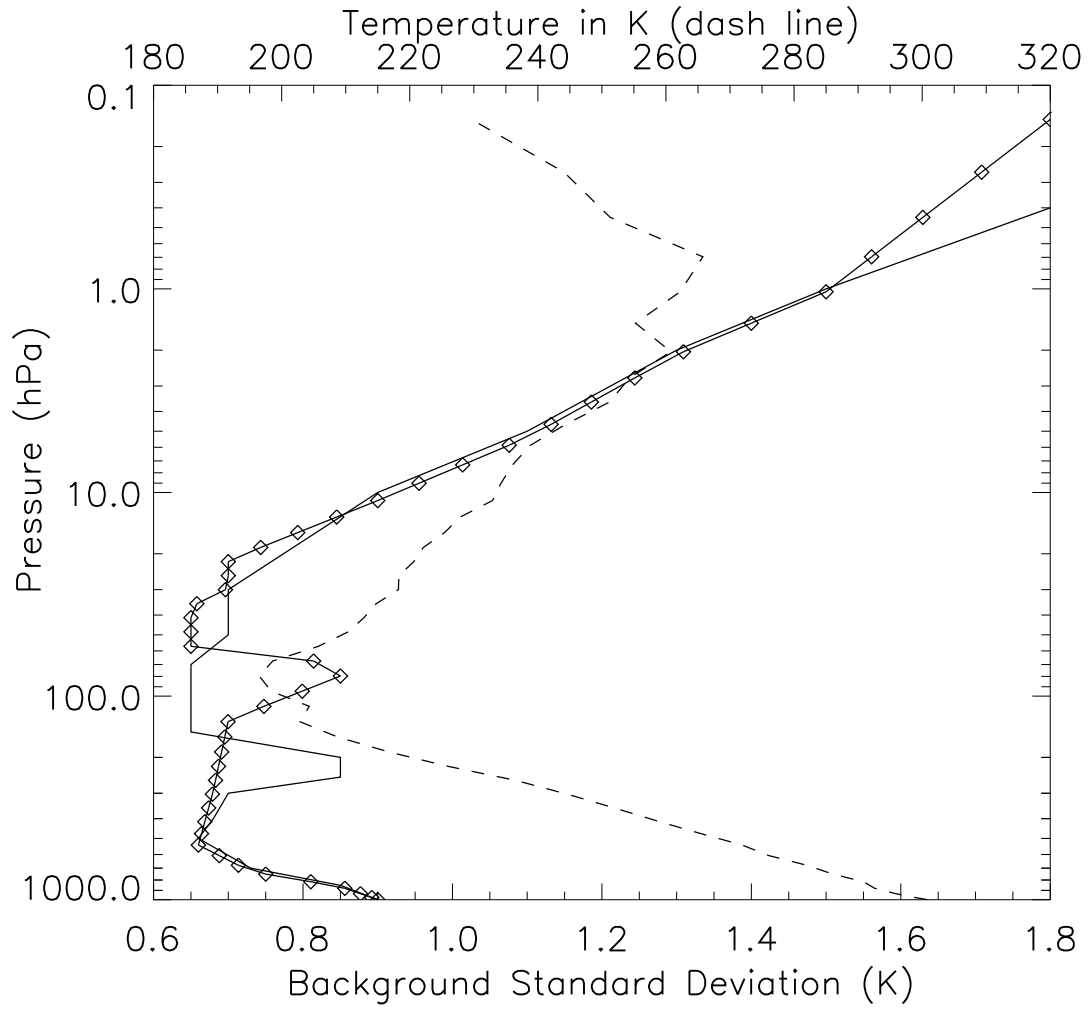
Figure 4: Assumed temperature errors for the background : *solid line* : for a tropopause at 250 hPa (typically mid and high latitudes) - *diamonds* : for the temperature profile with *dashes* (latitude 7°N).

Altitude of the lowest point	North	Tropics	South
5 km or less	81%	60%	94%
4 km or less	63%	42%	89%
3 km or less	44%	24%	80%
2 km or less	24%	4%	60%
1 km or less	10%	1%	41%

Table 1: Percentage of occultations penetrating the troposphere down to a low altitude in the GPS/MET 1995 June-July data. 'North' designates latitudes between 30°N and 90°N, 'Tropics' 30°S-30°N and 'South' 30°S-90°S.

are indicative of forecast accuracies over data rich areas (such as North America) or future data assimilation systems, current accuracies over areas such as Southern hemisphere oceans are lower. Therefore, the impact the GPS data can have on the analysis may be somewhat underestimated. However, we also did an experiment in which we multiplied the background temperature errors by a factor 2 with the GEOS Assimilation. The comparisons with radiosondes (to be shown later) were virtually unchanged.

For humidity, we assumed different sets of variances. In the rest of the paper we will always state clearly what background error estimates are used. For the humidity error inter-level correlation only the term representing the exponential decrease related to the vertical distance between two levels in (8) is taken into account.

We assume a sea level pressure error standard deviation of 2.5 hPa. We also neglect cross-correlations between the different variable types in the background (temperature, humidity, and sea level pressure).

5.4   The GPS Observations

During the GPS/MET mission, there were some time periods when the Anti-Spoofing (A/S) encryption was turned off by the United States Department of Defense (US-DoD). We used the data from one of these, called 'Prime Time 2' from June 21st to July 4th 1995. We chose this period because the software then on the receiver enabled tracking the occultations deeper in the troposphere [*Kursinski and Hajj,* 2000]. Table 1 shows the percentage of occultations which probed the troposphere down to 5 km altitude or less; this number is higher in dry regions such as the Southern hemisphere (winter) than in the Tropics. The GPS data used here were processed by the Jet Propulsion Laboratory [Kursinski et al., 1997]. The locations of the 797 occultations of the data set are shown in Figure 5.

We assumed the following errors in the refractivity data : 1% below 5 km, 0.2% up to 30 km, based on the estimations of *Kursinski et al.* [1997]. Above 30 km, several sources of error, negligible in the troposphere, become gradually more important as the refractivity becomes very small [*Kursinski et al.,* 1997]. *Hocke* [1997] identified "wave-like structures" in the upper stratosphere in GPS retrieved temperatures. Since we cannot determine whether these are real or result from errors in the observations, we simply chose not to give weight to the GPS refractivity observations above 30 km, and assigned a 50% error in refractivity above that altitude in the present analysis.
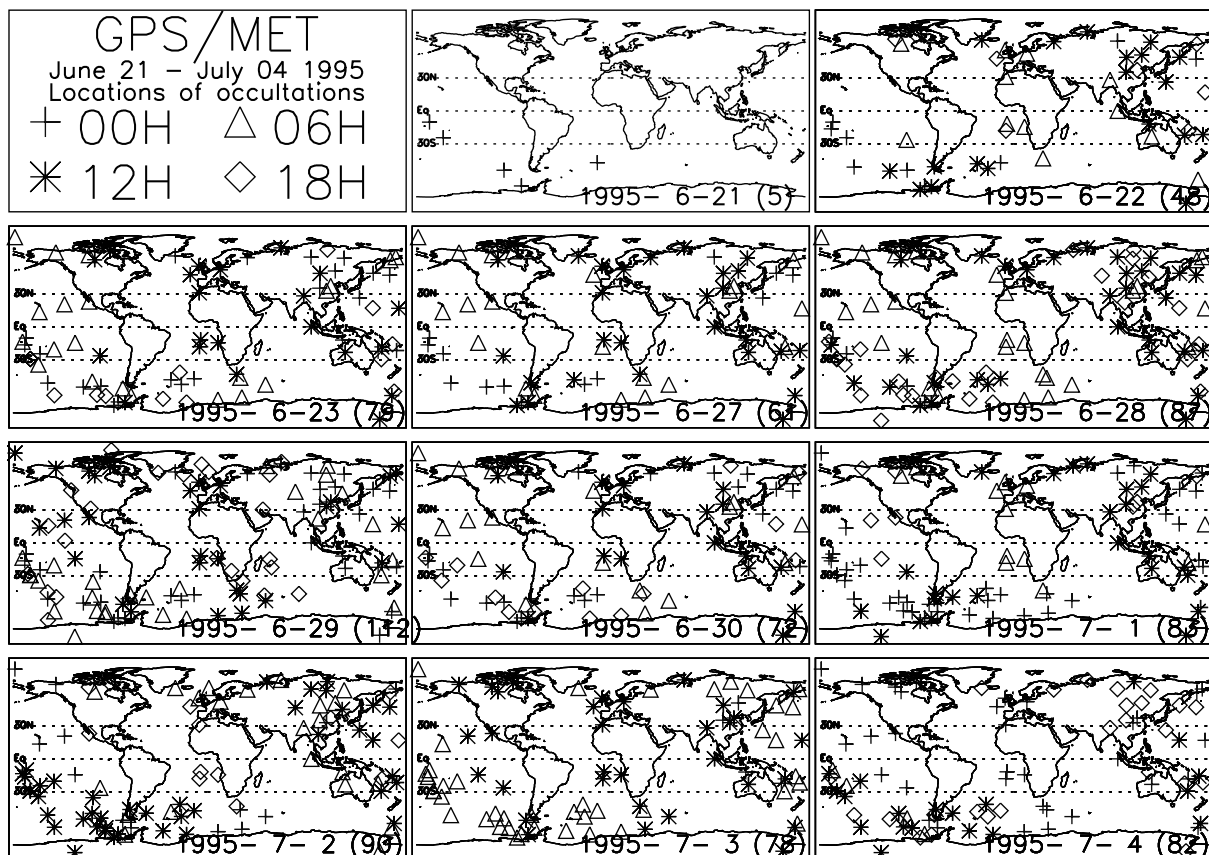
Figure 5: GPS/MET Occultations with no GPS encryption, June-July 1995. The chart is one map per day and the dates are shown at the bottom of each map, with the number of occultations for the day in parentheses. Different symbols are used for different synoptic periods.

13

We incorporate inter-level observation error covariances using a Gaussian-type decrease:

$$Cov(N_i, N_j) = \sigma_{N_i} \sigma_{N_j} \exp\left(-\frac{(z_i - z_j)^2}{\Delta L_i \Delta L_j}\right), \tag{9}$$

where $Cov(N_i, N_j)$ expresses the refractivity error covariance between two levels i and j, σ_{N_i} is the refractivity standard deviation for the refractivity observation N_i. The scale height ΔL_i depends on the spacing of the two levels surrounding the observation altitude z_i:

$$\Delta L_i = \frac{1}{4}(z_{i+1} - z_{i-1}). \tag{10}$$

This formulation was derived empirically and enables the observation error covariance matrix to remain positive definite even when the refractivity observations are very close (500 meters vertical spacing or less). The idea is to avoid too strong correlations, while still correlating adjacent measurements.

5.5 The Observation Operator

The observation operator converts temperature, humidity, and pressure profiles into refractivity profiles expressed as a function of altitude. It contains the physics of the measurement and an appropriate space-time interpolation. We assume here that all observations happen at the synoptic time for which our background estimate is valid. The background profile at the observation location is obtained by interpolating bilinearly between the model grid points. It follows that (1) computing refractivity and (2) mapping pressure levels onto altimetric levels are the two main features of this operator.

Instead of performing the analysis on the levels of the forecast, it is possible to work on more levels, for example the levels of the observations. Such an approach can yield analyzed profiles that account for the high resolution features detected by the GPS that cannot be represented by a relatively coarse analysis [*Kursinski et al.*, 2000]. However, the profiles are to be assimilated in a global circulation model (GCM) and thus can be brought back to a lower vertical resolution more consistent with the model's dynamics. This is the reason why we choose to work on the levels of our background information. Moreover, the computational cost of analyzing on 18 or 46 levels is much smaller than the typical 60-90 observation altitudes.

There are two different ways of performing the forward operation : (1) computing refractivity at each model level, then interpolating refractivity profile expressed in pressure levels into a profile expressed in altimetric levels ; (2) interpolating model variables from each pressure level to the altitudes of the GPS observations, then computing at each point the refractivity value.

Since our goal was to obtain the best profiles for further assimilation, we choose to calculate refractivity first and to interpolate it after. This requires only one interpolation. In addition, calculating refractivity with interpolated values for temperature and water vapor content makes the Jacobian more complex.

Refractivity values are computed for each model level. For each of these levels, the altimetric altitudes are calculated using a hydrostatic integration. Assuming $P_{sealevel}$

corresponds to 0 meter altitude, the refractivity values are interpolated to the altitudes of the observations using a linear in log of pressure interpolation scheme.

5.6   Linearized Version of the Observation Operator

In (6) we must not only have an observation operator h, but also its Jacobian H, the partial derivatives of the observation operator with respect to the various elements of the state vector. We derived an analytical formulation for H. As a check, it was compared with a computation by finite differences as in [*Eyre et al., 1993*].

The refractivity at one level is sensitive to a variation in temperature and humidity at that level and under that level. This is the result of the altitude calculation using hydrostatic integration starting from the surface. A change in the state vector at a given altitude has no influence on the simulated refractivities located below, but influences the altitudes of the pressure levels above, and hence the refractivity. Figure 6 shows a few columns of the H matrix.

A positive perturbation in temperature corresponds to a decrease in refractivity at the same level. It has no influence on the calculated refractivities at lower altitudes. The value of the refractivity at each pressure level located above does not change. However, due to the increase in temperature and hydrostatic integration, all the pressure levels above are moved to higher altitudes. This shifts upwards the upper part of the refractivity profile versus height, and increases refractivity for a given altitude.

Increasing humidity increases the local refractivity (the plot is for $-log(q)$). It has only very little influence on other levels through the hydrostatic integration.

The sea level pressure has no direct influence on the refractivity values of each model pressure level. However, it increases the pressure difference between each model level and the sea level, which is the equivalent to increasing the altitudes. The final effect of a positive perturbation in sea level pressure is hence to increase refractivity for a given altitude.

6   Theoretical Improvement of GPS Data over Background Information

With an estimate of the errors contained in the GPS measurements and the background, it is possible to estimate the improvement in an analysis due to these data without having real GPS observations, using, for example, (1) linear methods from *Rodgers* [1990] and (2) fully non-linear Monte-Carlo simulations. The first method does not require simulated observations. The results given by both methods must be viewed with some caution, because of the assumptions: e.g. no bias, no assumed correlation of errors of the different types of variables, and perfectly estimated background and observation Gaussian errors. In order to evaluate the robustness of the results, we applied various error estimates and different climatological conditions.
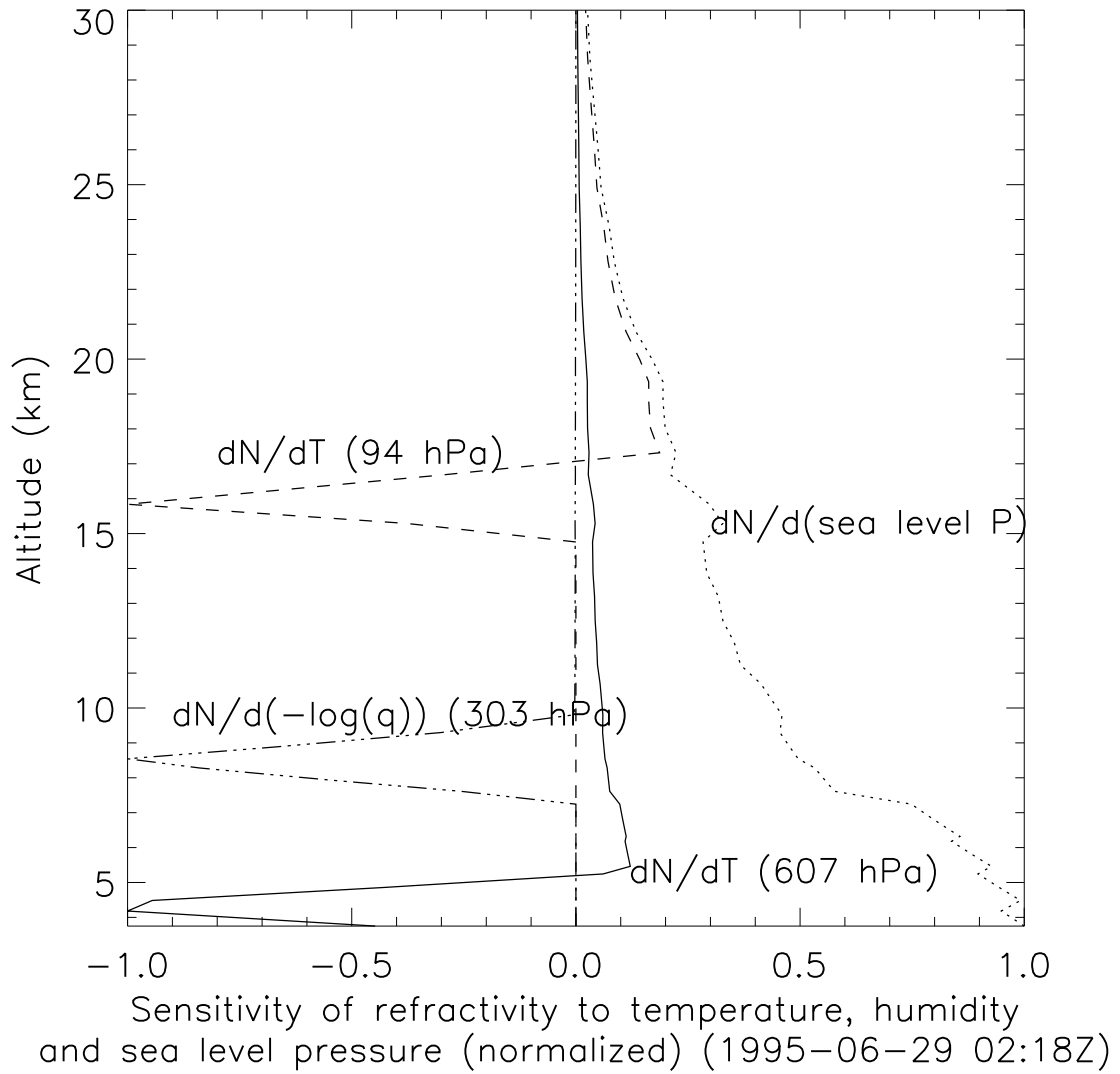
Figure 6: Jacobian for the GPS 1DVAR. Curves for temperature at 607 and 94 hPa, for humidity at 303 hPa, and sea level pressure.

6.1 Experimental Design

6.1.1 Linear Analysis

Under the hypothesis of linearity and zero-mean Gaussian error distributions, the error covariance matrix of the analysis P^a is given by

$$P^a = \left(H^T R^{-1} H + B^{-1} \right)^{-1},\tag{11}$$

[e.g. *Rodgers*, 1990]. The elements on the diagonal represent the variance of the solution with respect to the 'true state' that we try to estimate.

6.1.2 Monte-Carlo simulations

These are carried out in order to confirm the linear results and to test the 1DVAR. In each experiment, 1000 atmospheric profiles are created. A basic atmospheric profile (the "truth") is perturbed. The direction of the perturbations originate from the eigenvectors of the background covariance matrix. In each orthogonal direction, the intensity of the perturbation is obtained by multiplying the corresponding square root of the eigenvalue by a random number (normal distribution). Finally, the sum of all the perturbations and the original "true state" gives the background estimate.

For the observations we assume a GPS refractivity vector containing 56 elements, from 1 to 56 km altitude. For the background we use information on 18 pressure levels, and assume for the moment that the sea level pressure is correct (i.e. not included in the state vector). Later in the paper we evaluate the impact of adding errors to the background sea level pressure.

6.2 Conservative Error Estimates

In this section we assume observation errors of 2% below 5 km and 0.2% above (up to the top). We overestimate the errors in GPS data in the lower troposphere: 2% instead of 1% estimated by *Kursinski et al.* [1997]. This provides a conservative estimate of the impact the GPS may have on the analysis. To gauge the influence of the latitude, we use the same model-generated atmospheric profiles as in *Joiner and da Silva* [1998]. In the calculations, we assume the same background errors for all latitudes. These errors, derived from *Joiner and Rokke* [2000], are shown in Figure 7.

6.2.1 Linear Analysis Results

Figure 7 shows the estimated temperature and humidity error standard deviation at various levels for the analysis (see legend as "Linear analysis"), for an atmospheric profile located at 30°N latitude, during the winter. According to the Figure 7, the analysis should present a net reduction of error in temperature, when compared with
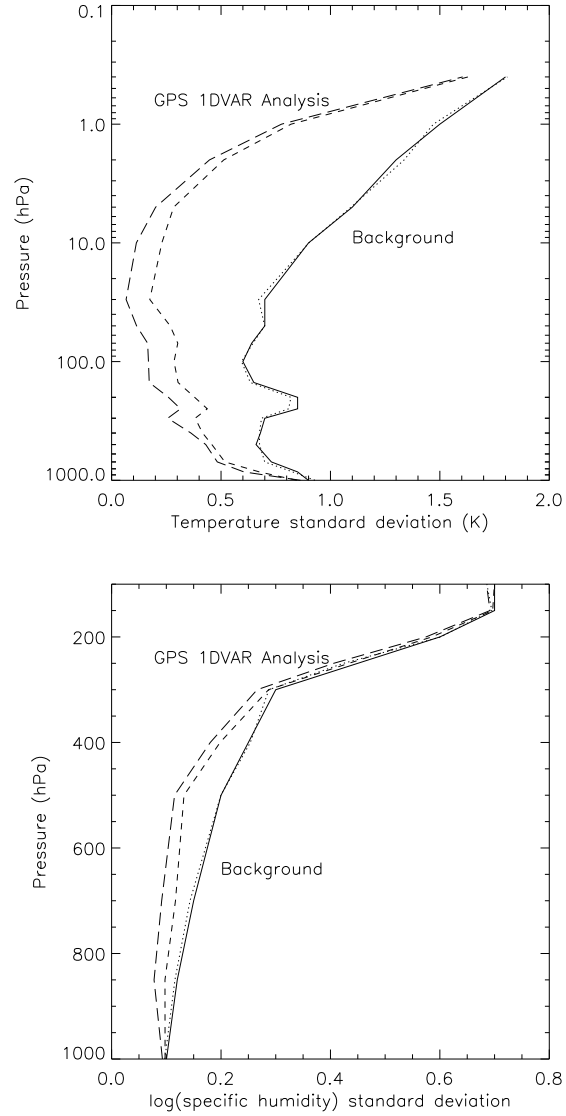
Figure 7: Standard deviation of : *top* : temperature ; *bottom* : log specific humidity. Solid line : assumed background errors ; dotted line : background errors generated in Monte-Carlo simulation ; short dashes : linear error analysis with observation errors ; long dashes : Monte-Carlo analyses errors (no errors added to the observations). Winter case, latitude 30°N.

18
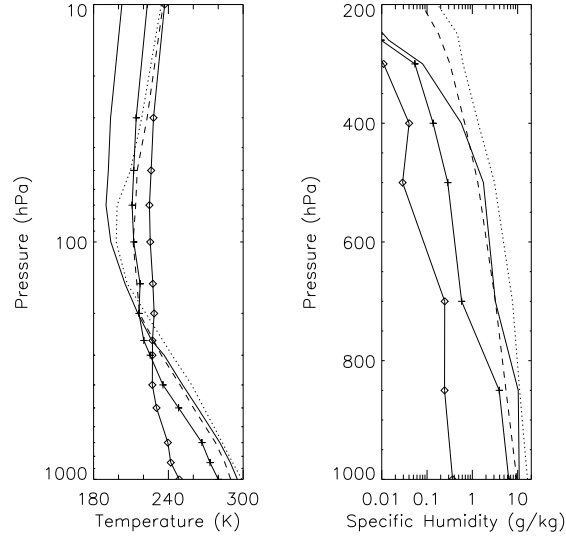
Figure 8: Atmospheric profiles used to perform the linear error analyses and Monte-Carlo simulations. *Solid line* is latitude 18°N, *crosses* and *diamonds* are winter conditions, 37°N and 63°N, respectively. *Dotted line* is a tropical profile, the curve with *dashes* is a mid-latitude summer profile.

the errors *a priori*. In terms of humidity, the expected improvement is relatively smaller.

For lower latitude conditions (e.g. 18°N profile in Figure 8), below the 400 hPa level, the water vapor content is important enough to play a role *via* the wet term in the refractivity in (4). This results in a larger reduction of humidity error in the analysis, as shown in Figure 9. But at higher latitudes and for winter conditions (37°N and 63°N profiles in Figure 8), the contribution of water vapor to refractivity is much smaller. Hence, GPS refractivity provides little constraint on water vapor. The retrieval is then not as accurate in deriving fractional water vapor content, and the analysis does not improve much upon the background humidity errors (see Figure 10). Concerning the temperature, the analysis has for all latitudes a significantly lower standard deviation error than the background, as shown in Figure 7.

6.2.2 Monte-Carlo simulation with no error added to the observations

In this first Monte-Carlo experiment the refractivity profile is taken as the exact result of the observation operator applied to the true state. No error is added. We ensure that 1000 profiles are sufficient to generate a distribution with no significant bias as assumed in the theory (e.g. after generation of the population the temperature bias is less than 0.06K). Figure 7 shows the statistical results of the experiment. They are better than that expected from the linear error analysis which assumed observational errors. This indicates that the impact of the observations can be overestimated if observational errors are not simulated in an OSSE.
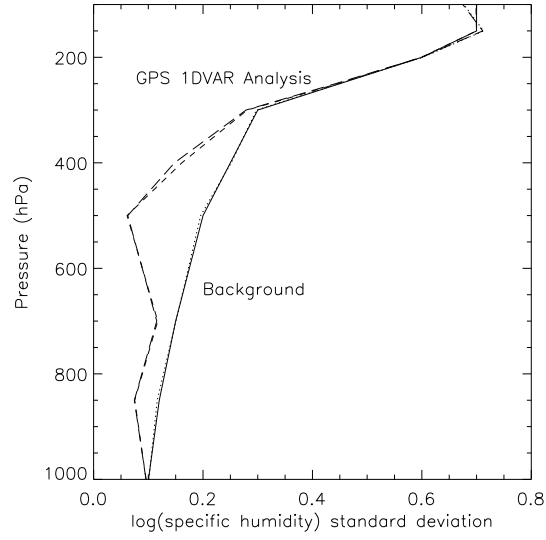
Figure 9: Standard deviation of log specific humidity, latitude 18°N. Curves are as described in figure 7 with the difference that noise is added to the observations in the Monte-Carlo simulation.

6.2.3 Monte-Carlo experiments with errors added to the observations

Here, the observed refractivity profiles are perturbed. Errors are added about the exact simulated refractivity obtained from the true state, using the eigenvalues and eigenvectors of the observation error covariance matrix R. Three experiments are conducted for the three different atmospheric profiles of the linear analysis.

Figures 9 and 10 (Figure 11) show a good agreement with the humidity (temperature, respectively) linear error analysis results. We have also shown that the 1DVAR works correctly with simulated data. In all of 3000 analyses the 1DVAR algorithm converged.

To summarize, under winter conditions and with conservative error assumptions (i.e. we take some caution not to overweight the observations), refractivity data are expected to bring significant improvement for temperature at all latitudes. For the humidity, the best improvements appear in regions of relatively high amount of water vapor (i.e. Tropics, mid to lower troposphere).

6.3 How Refractivity Constrains the Retrievals

Figure 12 shows how the refractivity can constrain the errors in humidity and/or temperature very differently, in a more visual manner using the technique of *Kursinski et al.* [2000]. We assume that both observations and background information are non-biased, and that the altitudes of the considered pressure levels are known without ambiguity. Two very different cases are shown: tropical conditions at the 850 hPa level (specific humidity greater than 10 g/kg), and high latitude winter con-
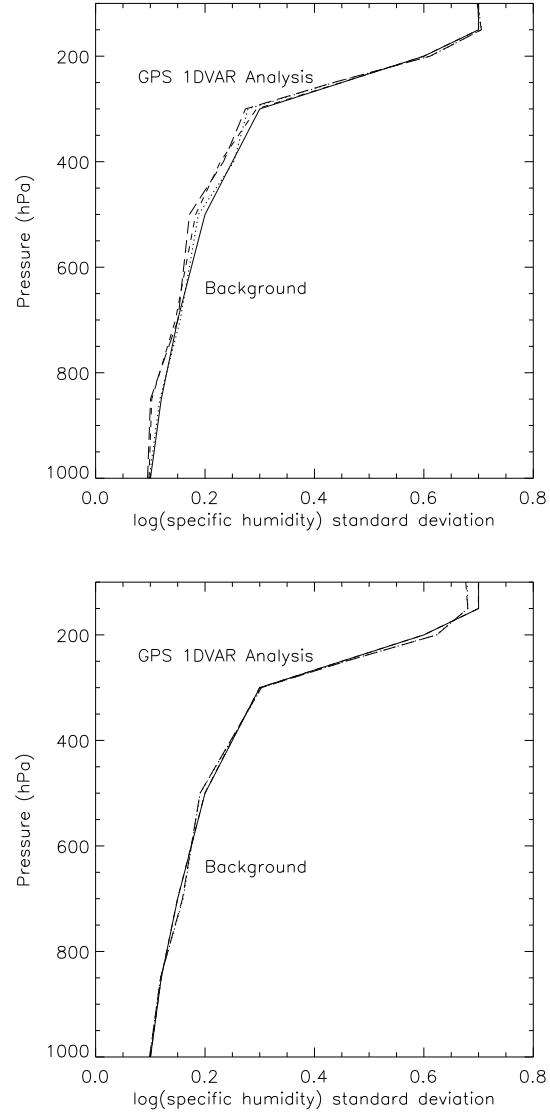
Figure 10: Same as figure 9, but for latitudes 37°N (*top*) and 63°N (*bottom*), winter cases.
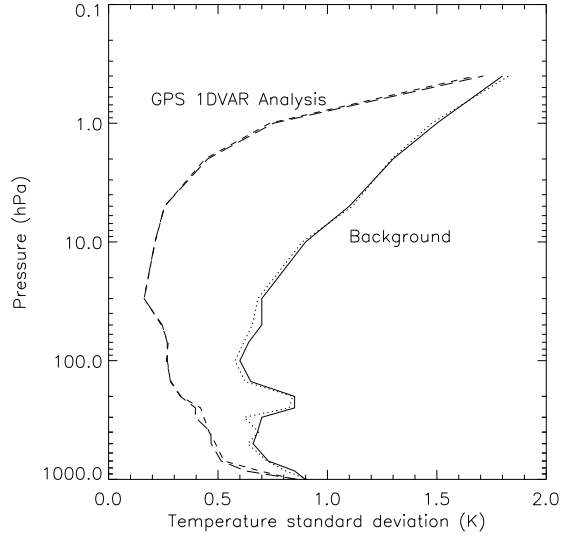
Figure 11: Same as figure 9, latitude 18°N, but for the temperature.

ditions at the 500 hPa level (specific humidity close to 1 g/kg). The knowledge of the refractivity gives a constraint represented in both cases by a tilted solid line of constant refractivity. The error in refractivity primarily shifts the center line into two extreme positions, 1% (for tropical cases, 0.2% for high-latitude cases) above or below the central refractivity value. The humidity (temperature) background errors are represented by the vertical (horizontal) error bars: 0.3 in log for the 850 hPa level and 0.4 in log for the 500 hPa level (0.85 K and 0.66 K for temperature, respectively).

For the tropical case, the refractivity line is nearly horizontal. This constrains the humidity estimate to an uncertainty smaller than the background error. The uncertainty in temperature (about 1.5 K) remains larger than that of the background (0.85 K). It is important to note that properly assimilating such analyzed temperature into a DAS would still add a little bit of information. For the other case (i.e. high latitude winter conditions), the constant refractivity line is tilted significantly towards the vertical. Therefore, the uncertainty in specific humidity is only slightly reduced over the background. The reduction of error in temperature is now more significant.

The middle and high latitude profiles used to perform the previous Monte-Carlo and linear error analyses correspond to rather dry conditions (in the specific humidity sense, i.e. lower number of water molecules) similar to that which would be observed in the winter. During the summer, more water would be present in the atmosphere. We hence conduct a new analysis under summer conditions.

6.4   Modified Error Estimates

Based on the differences between the assumed observation errors (see section 6.2) on the one hand, and the analysis minus observation refractivity results (to be discussed later) on the other hand, we revisit here the potential impact the GPS data may

22
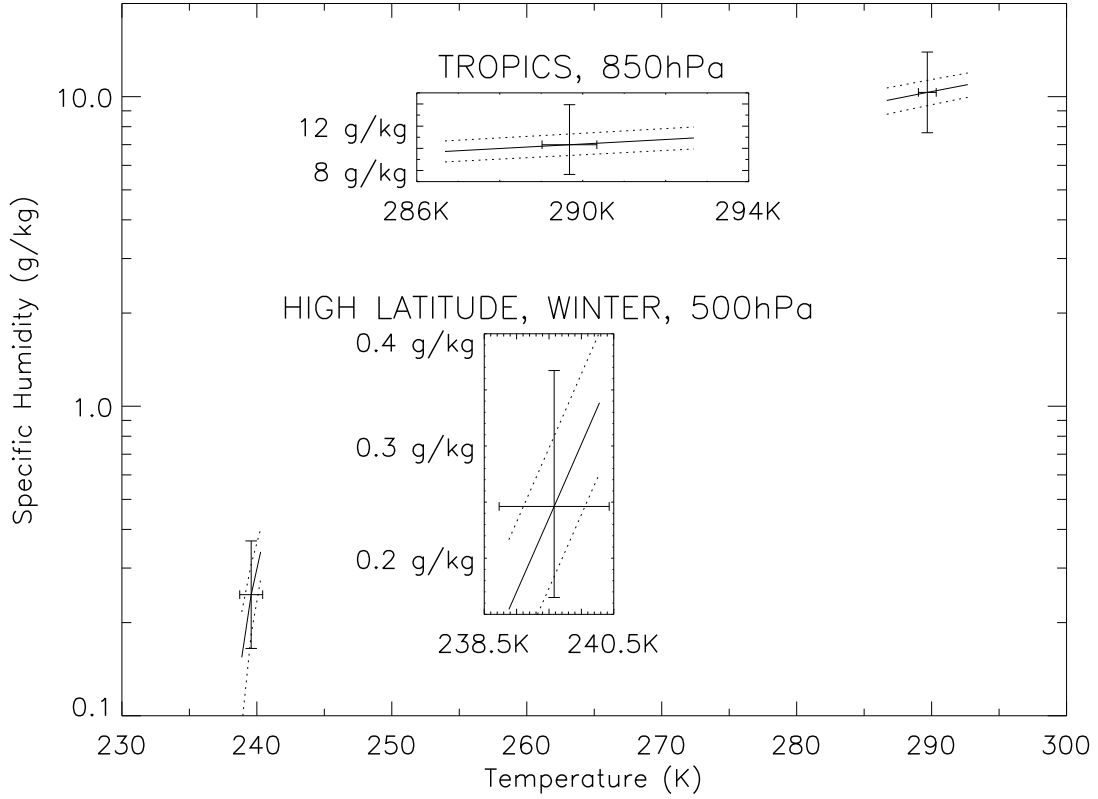
Figure 12: Illustration of the temperature and humidity constraints induced by a refractivity observation. The boxes show an enlarged view of two selected points. The two solid tilted lines represent the temperatures and humidity combination that would produce a constant refractivity. The dotted lines represent the spread in temperature and humidity due to uncertainty in refractivity. The vertical (horizontal) error bars are the errors of the humidity (temperature, respectively) background information.

have on the analysis of temperature and humidity. The refractivity residual standard deviation in Figure 24 (see explanation in section 9.1) is smaller than 2% below 5 km altitude, rather close to 0.4% in the North and 1% in the Tropics. Refractivity errors will be smaller than the refractivity residuals but we will use the residuals as an upper bound on the errors. At high altitudes, we have assigned a 50% error to the observed refractivity above 30 km.

For the background, we have assumed errors which are typically smaller than those of *Healy et al.* [2000] and *Palmer et al.* [2000], who have conducted similar simulation studies to evaluate the impact of GPS data on the quality of an analysis. Since our background errors may have been underestimated, we multiply the original background standard deviation errors by a factor of two, both for temperature and humidity. Background humidity errors below the 850 hPa level are assumed to be 0.3 in log of specific humidity to simulate specific humidity errors higher than 25% (see Figure 23). So we basically give more weight to the GPS observations in the lower troposphere, and remove nearly all influence of the GPS data above about 10 hPa.

Another restriction of the simulation studies shown above is that the sea level pressure was assumed to be known perfectly. We show here results of an experiment where the sea level pressure has been included in the state vector.

6.4.1 Mid-latitude, summer-type conditions

We choose an atmospheric profile observed during GPS/MET, located at 42°N and 30°W (June 29, 1995 at 12Z, see Figure 8). This profile is representative of the mean conditions for latitude 42°N for the GPS/MET 95 June-July period [*Kursinski and Hajj*, 2000].

Due to the good agreement between these the linear error analysis and a Monte-Carlo experiment based on 1000 profiles, we only show here the results of the Monte-Carlo simulation. The impact of the GPS on the humidity as depicted in Figure 13 is significantly larger than that in Figure 10 (note the change in the vertical scale between the two Figures). Reasons for the larger humidity impact are: increased background humidity errors, decreased GPS observed refractivity errors in the bottom 5 km (0.4% instead of 2%), and significantly higher specific humidity.

The impact on the temperature as shown in Figure 14 is not as large in the lower troposphere as in Figure 7 (here also note the change in the vertical scale). From 100 hPa to 30 hPa, the analysis temperature errors in Figure 14 are larger than that in Figure 7, which reflects the higher background errors. The degradation of the temperature analysis above 30 hPa due the increase in the observation errors from 0.2% to 50% is also apparent.

In order to account for an incorrect sea level pressure, we conduct another experiment which includes errors in the background sea level pressure (assumed error standard deviation: 2.5 hPa, with no bias). After performing the Monte-Carlo simulation the analysis sea level pressure error is reduced to 2 hPa, which is fully consistent with the result of a linear error analysis (square root of the last diagonal element of the P_a matrix with the state vector expressed in equation (7)). Figure 13 shows that the reduction of error in humidity is nearly unchanged as compared to the experiment when no error was added to the sea level pressure. In terms of temperature, the impact of the GPS refractivity data is slightly reduced in the lower part of the troposphere
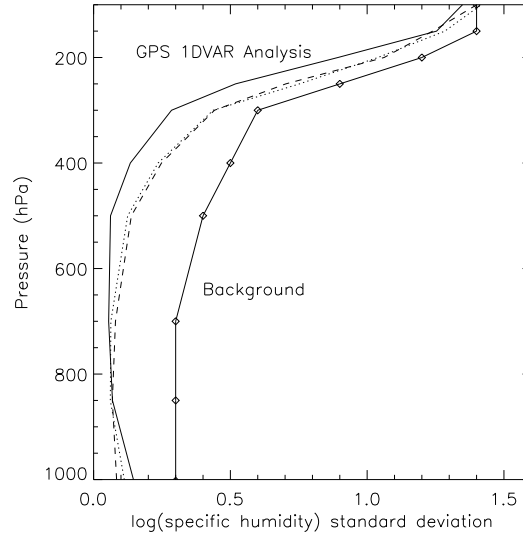
Figure 13: Impact of GPS on the analysis of humidity with different background and observation errors as explained in the text. *Diamonds* : assumed background errors ; *solid (dotted) line* : Monte-Carlo simulation for a tropical profile (summer mid-latitude profile, respectively). *Line with dashes* is the same as dotted line but with errors added to the background sea level pressure.
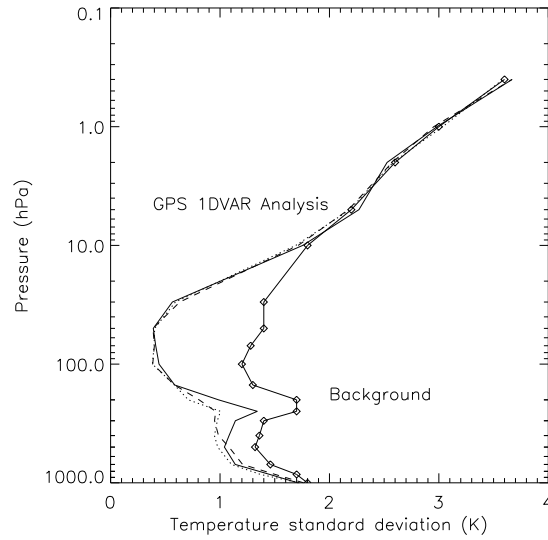
Figure 14: Same as figure 13 but for temperature.

when the background sea level pressure contains errors (see Figure 14).

6.4.2   Tropical conditions

We perform the same study as above but for tropical conditions such as those observed during GPS/MET, at latitude 11°N, longitude 123°E, on July 2, 1995 at 01Z. The assumed errors for the background are identical. However, for the refractivity, we specify an error of 1% below 5 km, accordingly to Figure 24. The following results rely on the assumption that the occultations can penetrate down to 1 km altitude in the tropics, which was infrequently observed during GPS/MET 1995 (see Table 1 for the June 21st-July 4th time period) but is expected to become more common with the new missions.

Figure 13 shows the humidity impact. On the one hand, the tropical conditions present higher specific humidity than in the mid-latitude summer (see Figure 8, tropical profile). On the other hand, the assumed observed refractivity errors are higher in the lower 5 km (1% instead of 0.4%). The net result is a larger humidity impact in the upper troposphere for the tropical profile than for the mid-latitude summer case.

In terms of temperature, the result is reversed: Figure 14 shows that the temperature impact is lower in the tropics than it is for mid-latitude summer conditions as explained in section 6.3.

To summarize, the impact of GPS is significantly modified when different error estimates are used. Under winter conditions and with conservative error estimates, the weight given to the GPS data is relatively small and improvement is mainly observed in terms of temperature. With summer mid-latitude conditions and error estimates that give more weight to GPS in the lower troposphere, the improvement in temperature is reduced but an improvement in analyzed humidity is observed. With tropical conditions, the improvement in humidity is always expected, but the temperature impact depends on the error estimates. Finally, we note that GPS always give a positive absolute impact in temperature and humidity, so a better background implies a better analysis.

6.5   Averaging Kernels

The repartition of information from a GPS 1DVAR analysis can be visualized using the concept of averaging kernels [*Rodgers*, 1990]. They are computed the following way: (1) for temperature, a 1 K impulse is added in the state vector at a single level, (2) the observation operator is applied to that state of atmosphere to obtain a refractivity profile which contains the 1 K impulse, (3) we perform a 1DVAR analysis using the unperturbed state vector for the background, (4) the difference between the retrieved temperature and the original state vector gives the response of the system. This is repeated for each level of the background state vector. Figure 15 shows that the 1DVAR analysis does not significantly spread the input impulse.

In the given example, the GPS observations start at 4.8 km altitude. The state vector is shortened so that the background information of only the levels located above the lowest GPS observation are modified by the analysis, as mentioned in section 5.2.
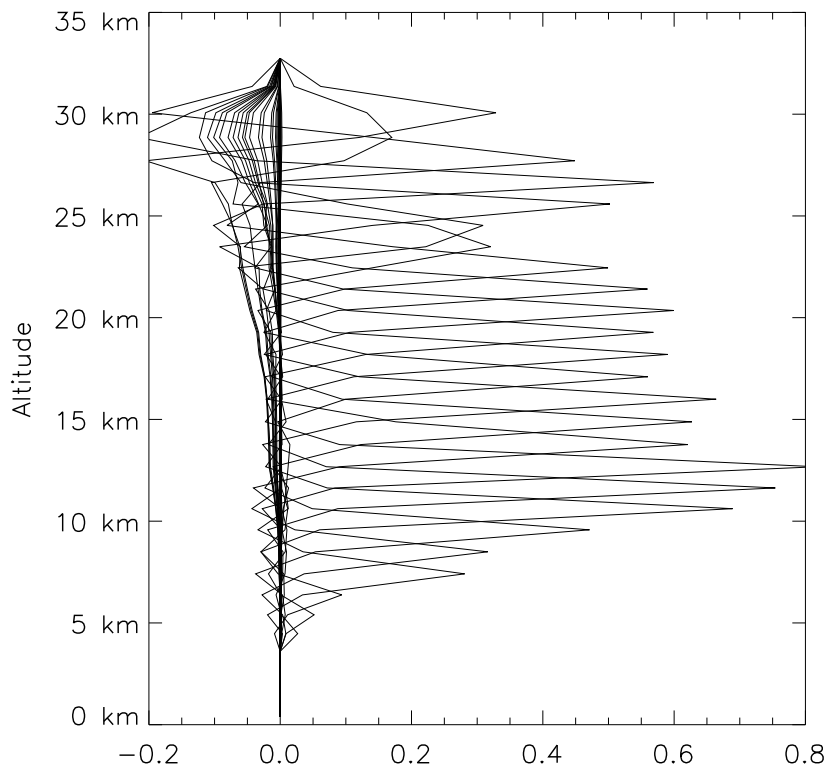
Figure 15: Temperature averaging kernels for the GPS 1DVAR, for an occultation reaching down to 4.8 km altitude.

Consequently the averaging kernels shown in Figure 15 start at 4.8 km.

A linear formulation of the averaging kernels is

$$A = D_y H, \tag{12}$$

[*Rodgers*, 1990], where A is a matrix containing the averaging kernels and D_y is the contribution function. D_y can be evaluated from

$$D_y = \left(H_i^T R^{-1} H_i + B^{-1} \right)^{-1} H_i^T R^{-1} \tag{13}$$

[*Rodgers*, 1976]. We checked that the averaging kernels obtained by this method were consistent with the results shown in Figure 15. Also, we can verify from equation (13) that if no weight was given to the background (i.e. if B^{-1} was to equal the zero matrix), the response would be equal to the original unit impulse, and focused at the appropriate level only (A would be the identity matrix).

7 Sensitivity of the Retrievals to Various Parameters

We now apply the 1DVAR analysis to data collected during GPS/MET. We first look at a few individual cases and point out sensitivities of the retrievals to some physical parameters.

7.1 Sensitivity to the Number of Levels in the Background

We will now focus on a single occultation which occurred on June 21st 1995, at 00:03UTC, at (10°S, 168°W). Three relevant temperature profiles are discussed here : the background (also called first-guess estimate, a 6-hour forecast of the GEOS model), the analysis obtained through the 1DVAR retrieval, and the direct retrieval assuming an *a priori* humidity profile [*Kursinski et al.*, 1997]. We assume a refractivity error standard deviation of 0.2% because the refractivity data start at 6600 m altitude for this occultation.

7.1.1 Analysis on 18 levels

Figure 16 shows the result of an analysis performed with background information on 18 levels with the top at 0.4 hPa (GEOS Forecast). The 1DVAR works on the same levels as those of the background and hence the retrievals are also on 18 levels.

The fine resolution of the GPS measurements as inferred by the direct retrieval appears to produce some high frequency structure in the stratosphere. The 1DVAR tries to simulate this structure, as the observation errors are relatively small as compared with the projected background errors. However, due to the coarse resolution of
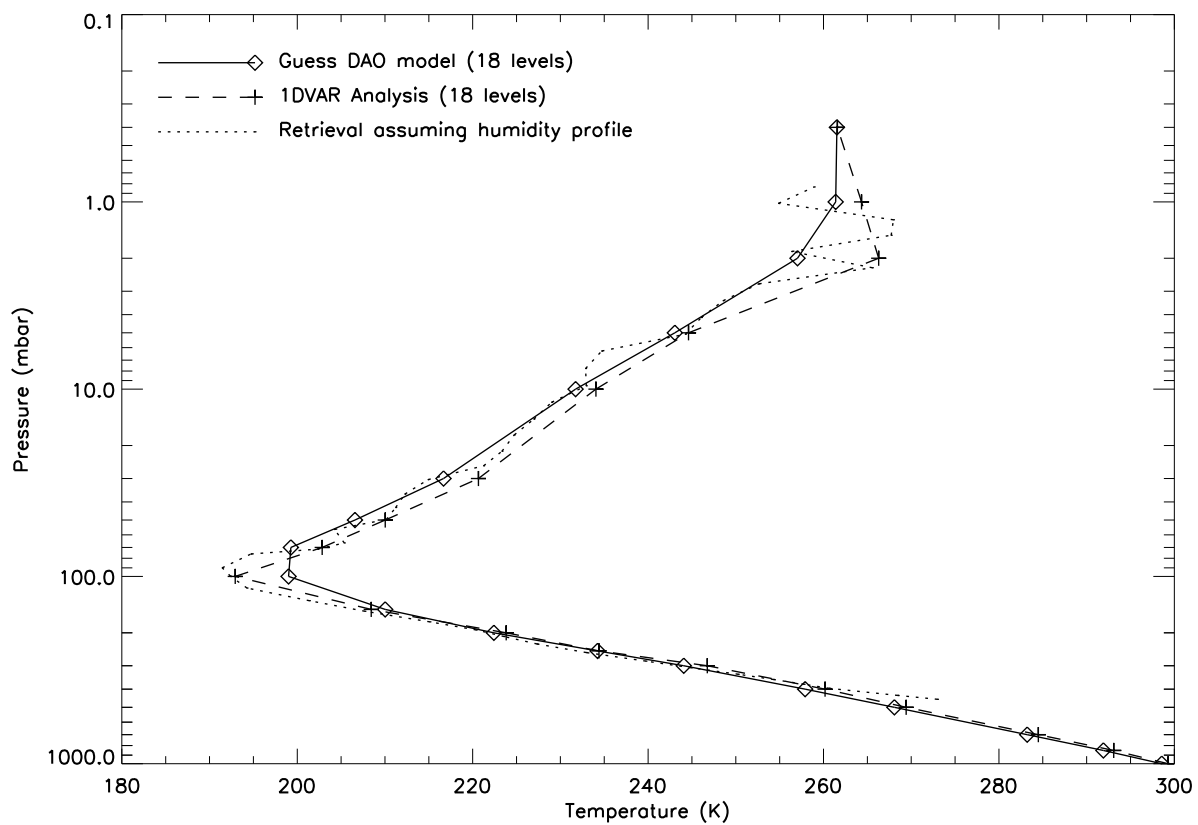
Figure 16: Temperature profile, 1DVAR analysis performed on 18 levels.
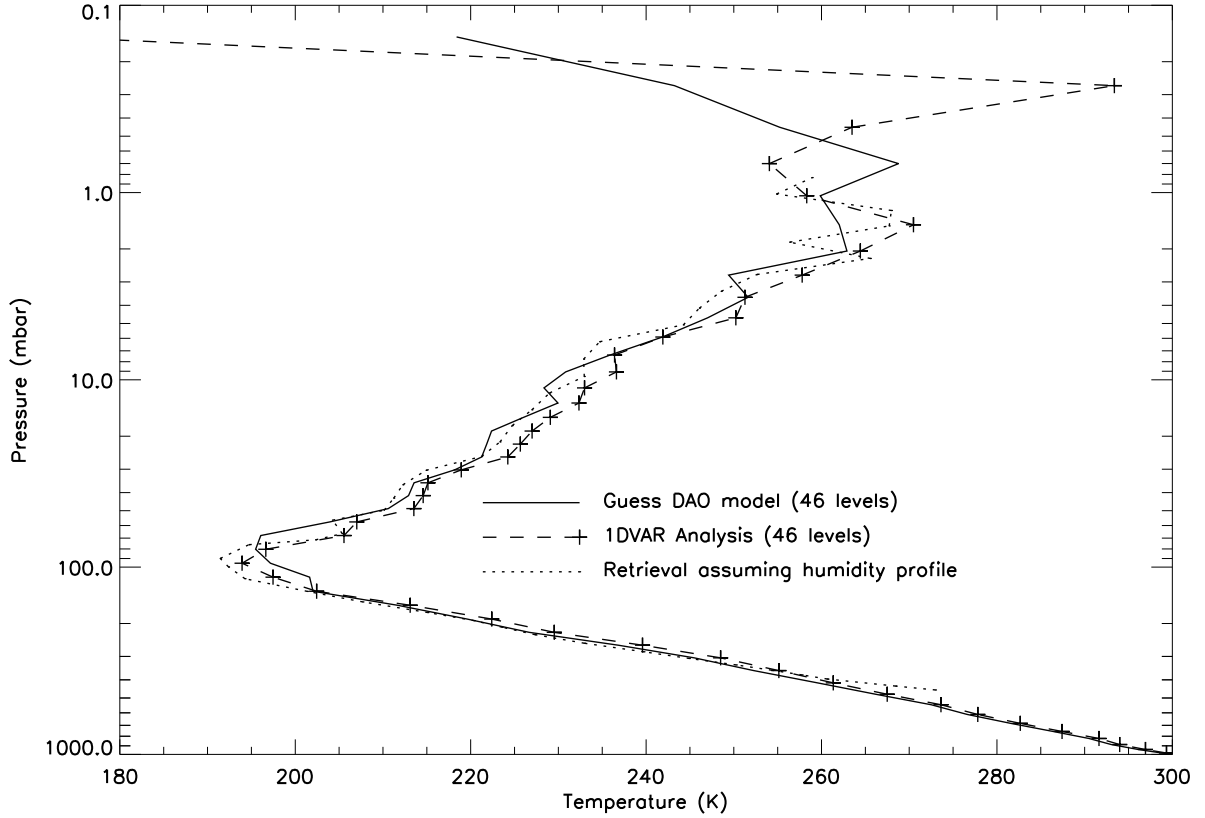
Figure 17: Temperature profile, 1DVAR analysis performed on 46 σ levels.

the state vector (based on the 18 levels of the background), the analysis cannot fully resolve the same observed structures as those seen in the direct retrieval.

The background used to perform the linear error analysis and Monte-Carlo simulation was on 18 levels. These studies did not take into consideration any inconsistency between the resolution of the observing system and the background. This inconsistency may be considered as representativeness error.

7.1.2 Analysis on 46 levels

In this analysis, the background information is specified on 46 σ levels, with a top at 0.1 hPa (GEOS Assimilation). We convert the σ levels to pressure. Figure 17 shows the result of the analysis of the same refractivity profile on 46 levels. We can see some "waves" in the analysis at this resolution. We also see a large increment at the top of the profile. As explained in section 5.4, we will subsequently increase the errors of GPS observations in the analysis above 30 km. Note that the structure at the tropopause is now much better resolved than before at low resolution. This demonstrates the need to analyze the GPS at a higher resolution than the GEOS-Strat analysis if the full impact is to be realized.

30

7.2 Sensitivity to the Gravitational Force

We found significant sensitivity of the analysis to the gravitational constant g used in the analysis. We used two formulations for g. (1) g=9.80665 m·s^{-2} (2) g=$g(altitude, latitude)$ [*List*, 1984]. The second gave better results by comparison with radiosondes (see next section for the final results).

Depending on the approximation used for the definition of g, biases of order 1K can appear. This sensitivity to the gravitational constant arises because the background and the GPS observations have different vertical coordinates (pressure versus altitude), and the translation from one to the other depends on gravity.

7.3 Sensitivity to the Reference Pressure

A boundary condition is needed to integrate the hydrostatic relationship. Here we define as 'reference' pressure the pressure at sea level. This reference pressure affects the computation of the altitudes.

The analysis increment is defined as the difference between the 1DVAR retrieval and the background, which is the GEOS Assimilation here. Figure 18 shows two different increments for the example of occultation 1995-06-28 at 09:31Z. The first one is calculated with a fixed reference pressure, i.e. the same as in the background estimate. In the second implementation, the reference pressure becomes part of the state vector and hence can be updated. The computed altitude of the level 10hPa is moved from 31,160 to 31,290 meters (after minimization) when the sea level pressure (SLP) cannot be moved by the analysis (i.e. the difference is created by the adjustment made on the temperatures). When the SLP is included in the state vector, the temperature increments are smaller, but the computed altitude is about the same as before at 31,280 meters.

Overall, radiosonde comparison statistics are improved when the reference pressure is adjustable. Adjusting the reference pressure allows the whole refractivity profile to be moved upwards or downwards. When it is not possible for the system to do that, it must increase or decrease the temperature in several layers to thicken or thin the layers, resulting in temperature errors of a larger vertical scale.

Adding this degree of freedom enables the 1DVAR to account for any inconsistencies that may exist between the background and the observations concerning the definition of the sea level. It may also limit the errors due to the interpolation of the sea level pressure from the background fields.

The sensitivity of SLP analyses to the lowest altitude of GPS measurements has also been evaluated by *Healy and Eyre* [2000] and *Palmer et al.* [2000]. Both found that error estimates of SLP derived from GPS radio occultation measurements were smaller in the case of occultations reaching lower altitudes.
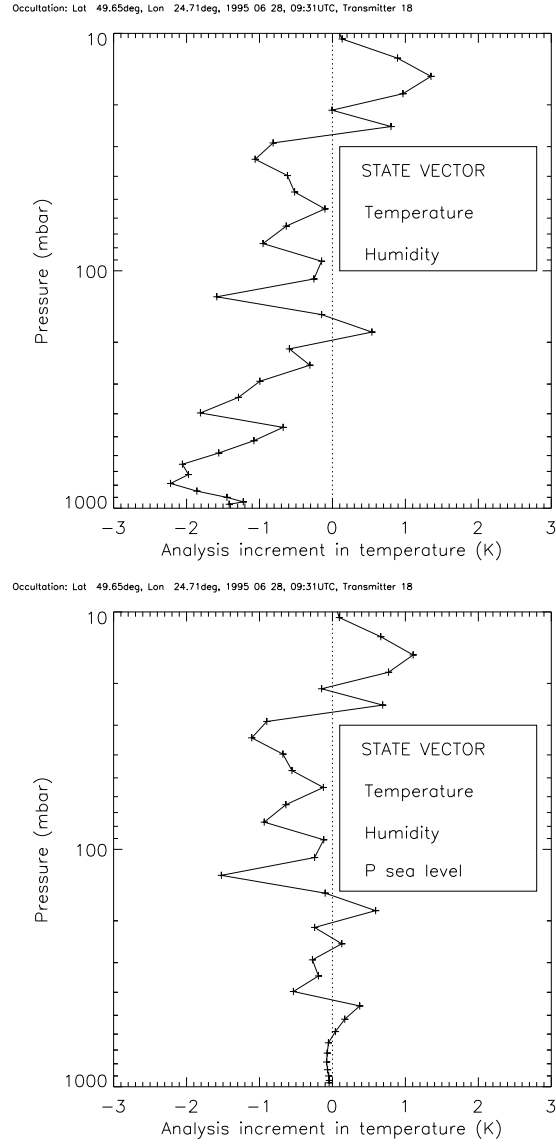
Figure 18: Temperature analysis increment. *Above* : sea level pressure of the background assumed as correct. *Below* : sea level pressure included in the state vector.

8   Comparisons with Radiosondes

In this section we compare results of GPS 1DVAR analyses with nearby radiosondes (RS), and discuss the statistics obtained.

8.1   Radiosonde Matches

The matching criteria are +/- 3 hours in time and less than 280 km in distance. The temperature (humidity) direct retrievals obtained using an estimate of humidity (temperature) [*Kursinski et al.*, 1997] are also shown, as well as the background used to perform the 1DVAR analysis.

Among the 797 GPS occultations, about 150 match the collocation criteria. Most of the matches occur in the Northern hemisphere, so we will focus on this region. Only one 1DVAR minimization process did not converge. As a background check, collocations with discrepancies more than 5 K between background and RS are removed from the statistics. It is necessary to apply some quality control to the RS and the direct retrievals. Therefore, we also remove discrepancies more than 5 K between the RS and the direct retrieval. No quality control is performed on the 1DVAR analyses themselves. Likewise, all specific humidity relative differences, background minus RS or RS minus direct retrieval, greater than 100% are removed.

8.2   Temperature

Figure 19 shows a single temperature profile which exhibits the advantages of combining information from a background and observations. (1) Both the direct retrieval and 1DVAR analysis are able to improve the tropopause upon the GEOS Assimilation. The background has a warm bias at the tropopause of about 5K. (2) In the lower layers, the analysis follows the background, whereas the direct retrieval notably diverges from the RS.

8.2.1   Background: GEOS Assimilation

Figure 20 shows the bias and standard deviation difference from nearby radiosondes for temperature in the Northern hemisphere (above 30°N) when using the GEOS Assimilation as a background. As a reminder, these GEOS profiles already contain some information from the RS (see section 5.3). The chart also indicates (to the right) the number of data used to calculate each point. That number decreases towards the surface because most occultations did not reach the surface as shown in Table 1. The balloon bursts above the tropopause explain the decreasing number of comparisons in the stratosphere.

All biases (GEOS background, GPS 1DVAR analysis, direct retrieval minus RS) are of the order of 1K or less below the 30 hPa level. The direct retrieval presents a larger (negative) bias than the GPS 1DVAR analysis above the 400 hPa level. Above 100 hPa, the negative bias of the direct retrieval is consistent with the results of

33

Occultation: Lat 58.94deg, Lon −65.88deg, 1995 07 03, 12:21UTC, Transmitter 16

Figure 19: Temperature profile showing the advantages of using a variational approach with GPS data. See text for explanation of regions (1) and (2). The background is the GEOS Assimilation.
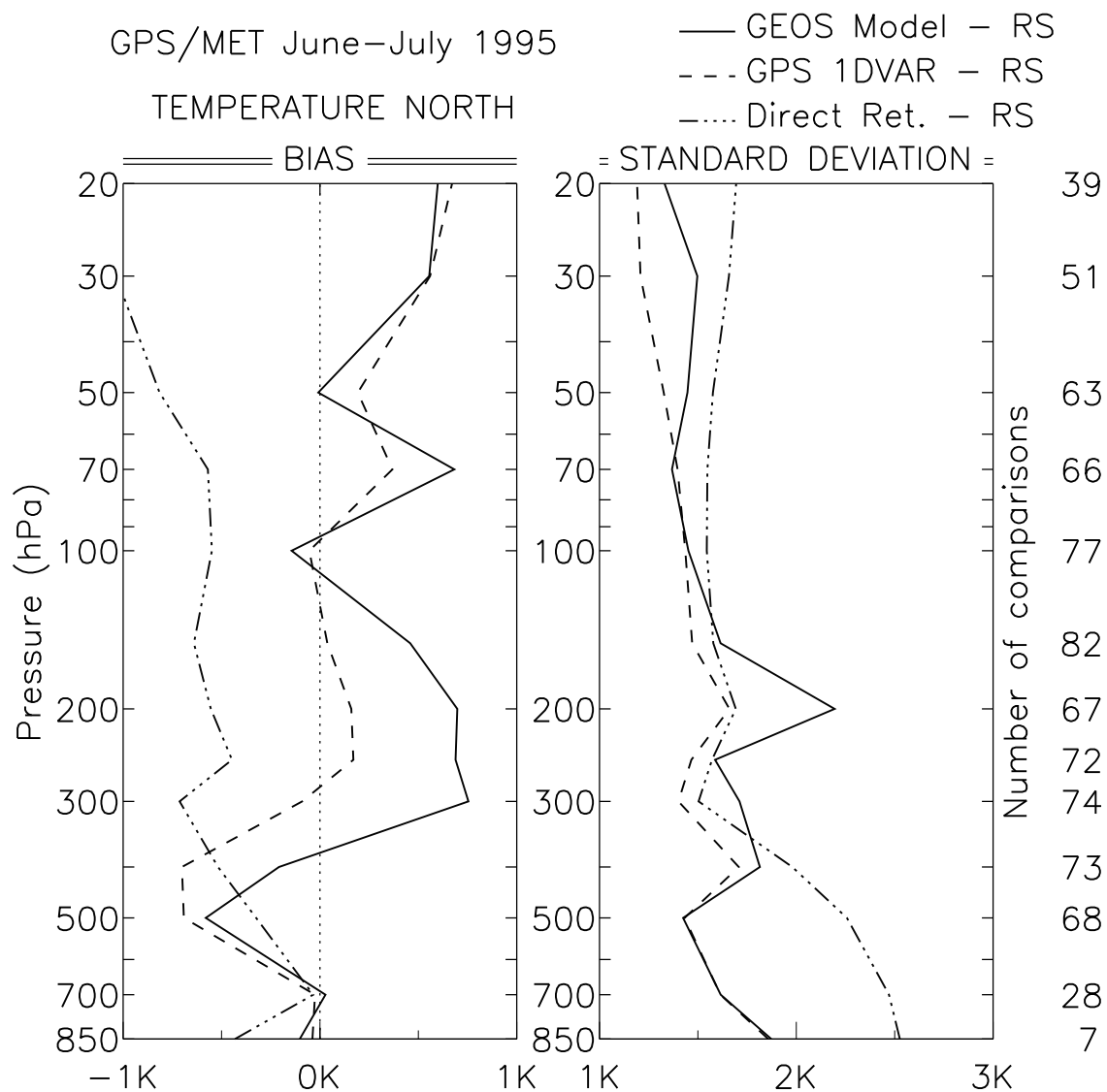
Figure 20: Northern hemisphere, comparisons with radiosondes temperatures (+/- 3 hours, less than 280 km) for the GPS 1DVAR, the GEOS Assimilation background and the direct retrieval. Curves show bias and standard deviation.

Leroy [1997] for the same period (Summer 1995). He observed a negative bias in the geopotential height derived from GPS as compared to ECMWF forecasts, which are tightly constrained by r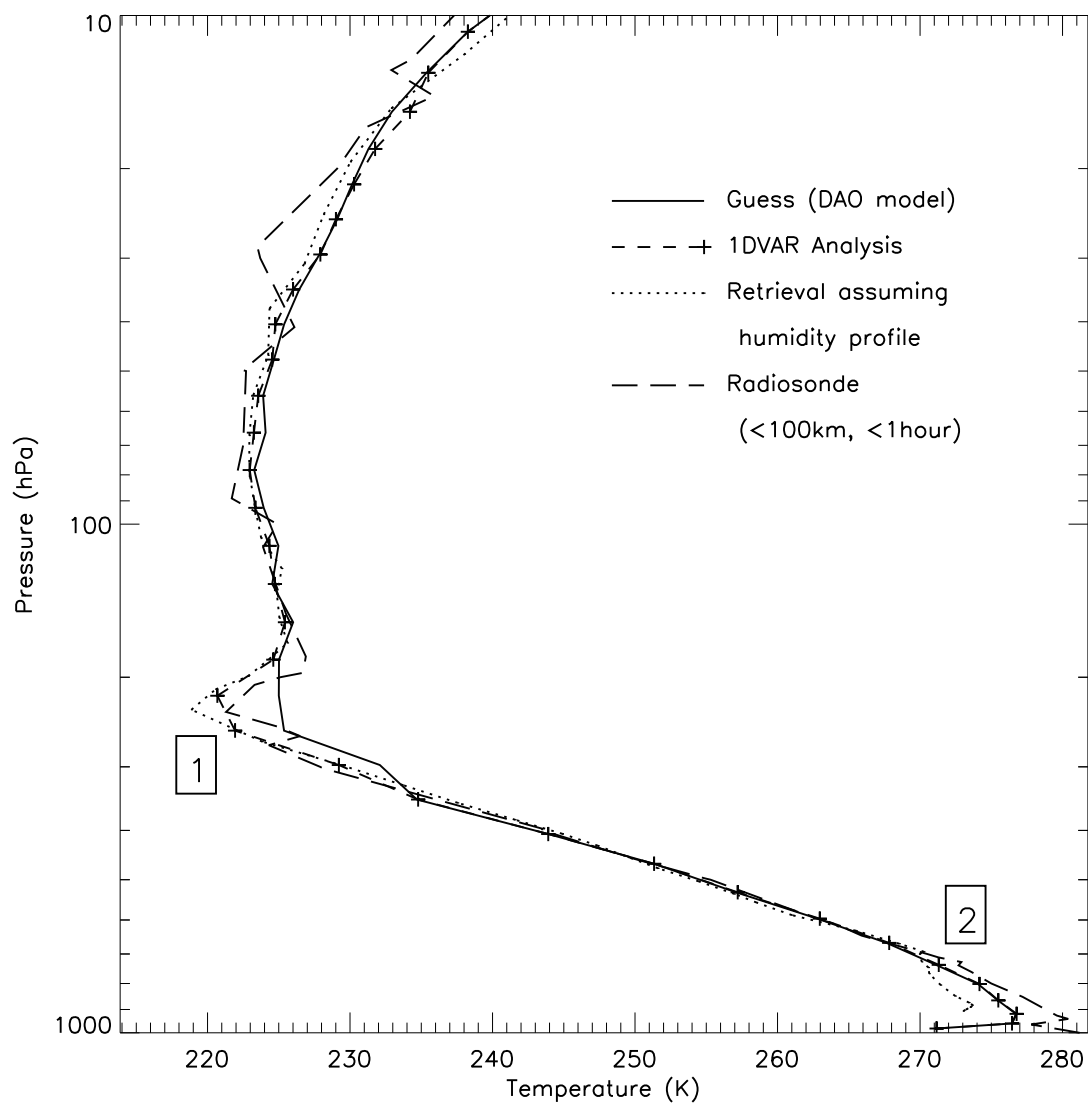adiosondes in the Northern hemisphere. Between 300 hPa and 100 hPa a significant temperature bias present at the tropopause in the GEOS background is reduced by the 1DVAR analysis.

The direct retrievals produce the largest standard deviations below the 400 hPa level (2.5K at 850 hPa). The 1DVAR analysis improves temperature standard deviation as compared with the GEOS Assimilation above the 500 hPa level (less than 2K), except around 70 hPa. The significant improvement of the direct retrieval and the 1DVAR analysis between 300 hPa and 150 hPa over the GEOS background (by comparison with the nearby RS) may be linked with a better description of the tropopause. Overall, the GPS 1DVAR minus RS temperature standard deviation is reduced as compared with the background minus RS at most altitudes.

8.2.2   Background: FVDAS NESDIS TOVS

Figure 21 shows the impact of the GPS refractivity on the analysis when using FV-DAS NESDIS TOVS forecasts as a background. We first notice that the numbers of comparisons with the RS have increased, indicating that there are fewer differences background minus RS more than 5 K.

The shape of the FVDAS temperature bias and standard deviation curves is similar to the GEOS Assimilation. Consequently, we note that the 1DVAR derived from the FVDAS NESDIS TOVS background presents the same characteristics as before, at least in regions where humidity plays a negligible role in terms of refractivity. A noticeable difference with Figure 20 is at the 400 hPa level: the background bias has gotten more negative, driving the 1DVAR in the wrong direction both in terms of bias and standard deviation.

8.2.3   Background: FVDAS DAOTOVS

As a reminder, the only difference between the FVDAS DAOTOVS and the FVDAS NESDIS TOVS is a change in the origin of the TOVS data assimilated into the DAS. Figure 22 shows the temperature differences FVDAS DAOTOVS background minus RS, as well as 1DVAR derived from this new background minus RS. The number of comparisons has increased again when compared with the FVDAS NESDIS TOVS, especially at 300 hPa (97 points instead of 90), indicating at that level a better performance for the forecast when compared with the RS.

The FVDAS DAOTOVS temperature bias above the 400 hPa level is less than 0.5 K, which is a significant improvement compared with FVDAS NESDIS TOVS. However, the negative bias previously present around the 500 hPa level has gotten more negative. The temperature bias plot in figure 22 shows that a change in the TOVS data assimilated in a model drastically changes the model-analysis temperature climatology.

The FVDAS DAOTOVS minus RS temperature standard deviations are less than 2 K throughout the entire vertical range (850-20 hPa). There is significant improvement

Figure 21: Same as figure 20 but with the FVDAS NESDIS TOVS background.
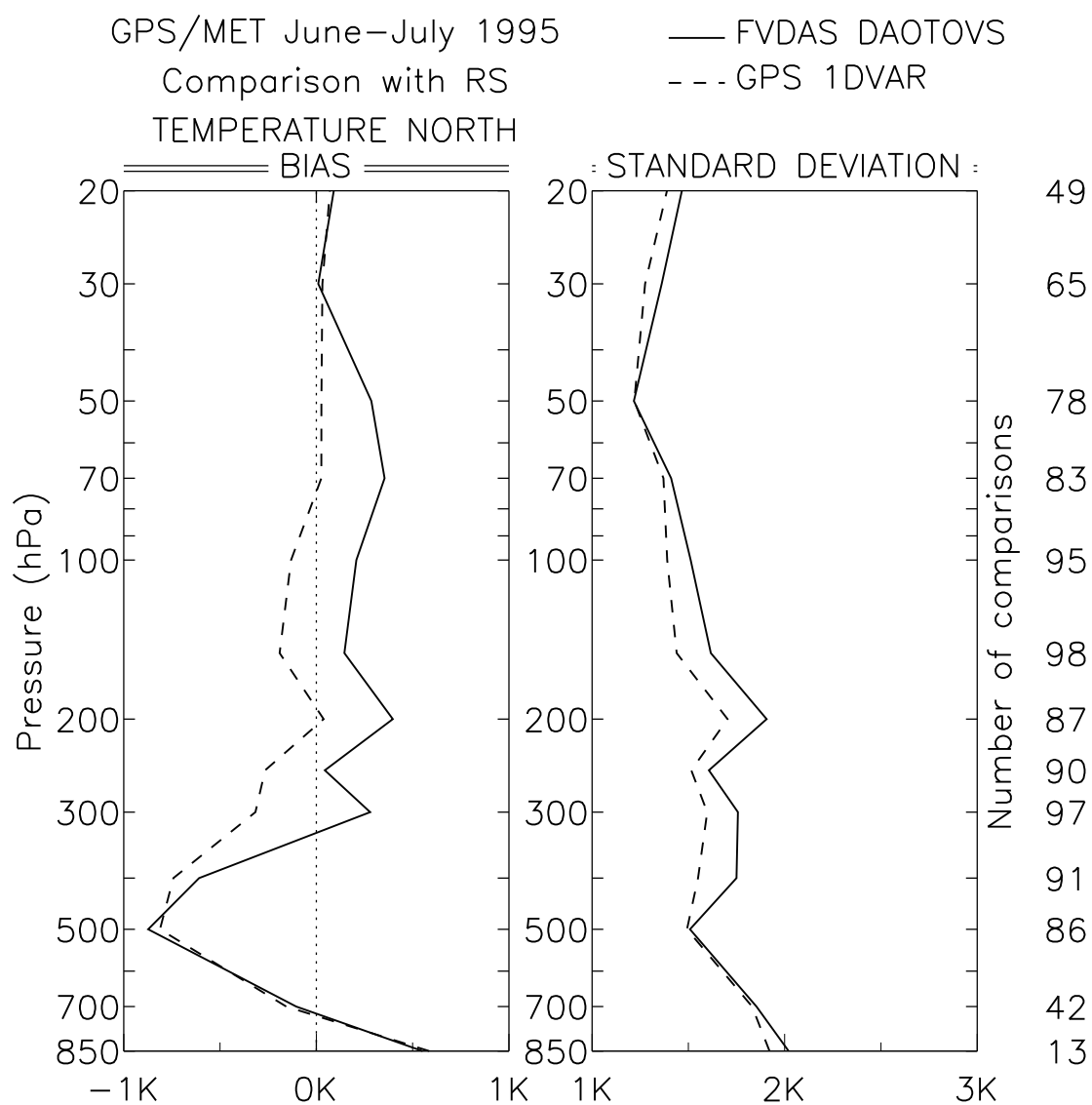
Figure 22: Same as figure 20 but with the FVDAS DAOTOVS background.

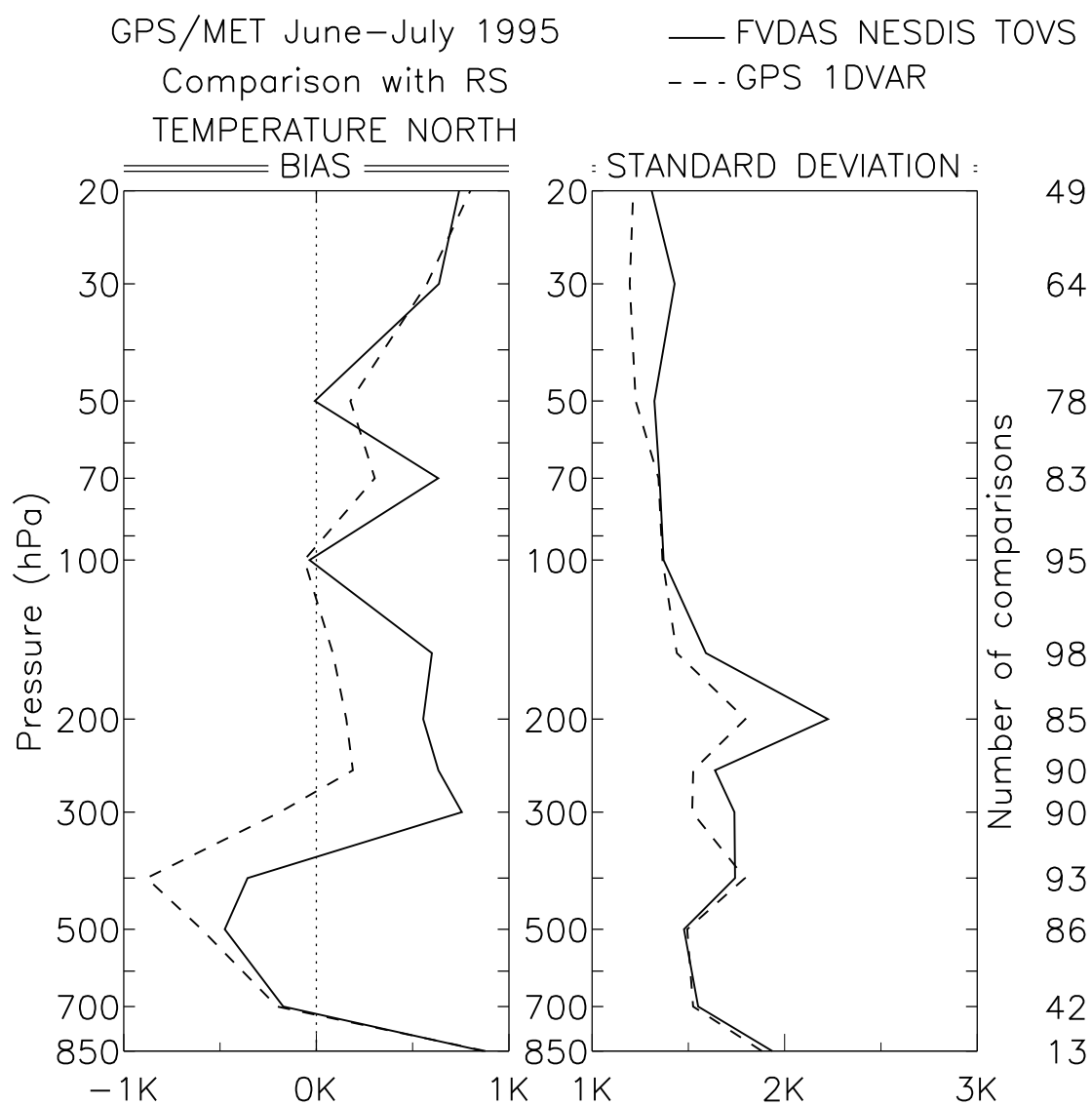| Pressure (hPa)	1000	850	700	500	400	300	250	200	150 and beyond
Log(q) std. dev.	0.40	0.40	0.40	0.20	0.25	0.30	0.45	0.60	0.70

Table 2: Assumed log of specific humidity errors for the background.

when compared with FVDAS NESDIS TOVS: the tropopause region is better described, and the bump in standard deviation previously observed around the 200 hPa level is smaller. The 1DVAR derived from DAOTOVS minus RS standard deviations are close to the ones of the 1DVAR derived from NESDIS TOVS above the 300 hPa level. In this region we can see that the *relative* impact in temperature of the GPS refractivity has been reduced with respect to the background we started with. Below the 300 hPa level, the temperature standard deviation improvement in the 1DVAR over the FVDAS background is extended, thus making now this improvement consistent throughout the whole vertical range of the profile (850 hPa-20 hPa). Near the surface, the GEOS Assimilation presents smaller standard deviation than FVDAS (note the small sample).

This clearly illustrates that the impact of GPS refractivity data upon a background issued from a DAS depends on the other data assimilated in the DAS; i.e. assimilating data types which help the forecasts fit to the RS reduces the relative positive impact of GPS refractivity upon the background.

8.3   Humidity

Table 2 shows the background humidity error estimates used here. They were modified after optimization by experiments as compared to the estimates from *Joiner and Rokke* [2000] used previously in section 6. In order to give more weight to the GPS data in the 1DVAR to move the humidities we increased the log of specific humidity error estimates from 0.1 (0.12, 0.15) up to 0.4 (0.4, 0.4, respectively) at the level 1000 hPa (850 hPa, 700 hPa, respectively).

Figure 23 shows humidity bias with respect to nearby RS for the global domain. We only discuss here the results obtained with the FVDAS DAOTOVS background because this was the only experiment in which TOVS humidity information was assimilated. This latter presents a bias less than 5% over the entire vertical range of the profile. The direct retrieval has a comparable bias -sometimes even smaller- in the 850-750 hPa and 600-450 hPa regions. The 1DVAR bias is usually the largest (negative), except at the 925 hPa and 400 hPa levels.

Figure 23 also shows that the FVDAS DAOTOVS is usually the closest to the RS point measurements in terms of standard deviation, with an increase from 20% at 925 hPa to about 45% at 450 hPa. The direct retrieval presents the largest standard deviation, except at the boundary levels shown on the plot (925 hPa and 400 hPa). The 1DVAR standard deviation globally stays in between the FVDAS and the direct retrieval. We can notice a slight improvement upon the background at the 650 hPa and 500-450 hPa levels.

Many radiosondes we used either did not report the humidity, or the reported humidity was different from the background and/or the direct retrieval by more than 100%. This results in a small number of comparisons. There are known problems with RS
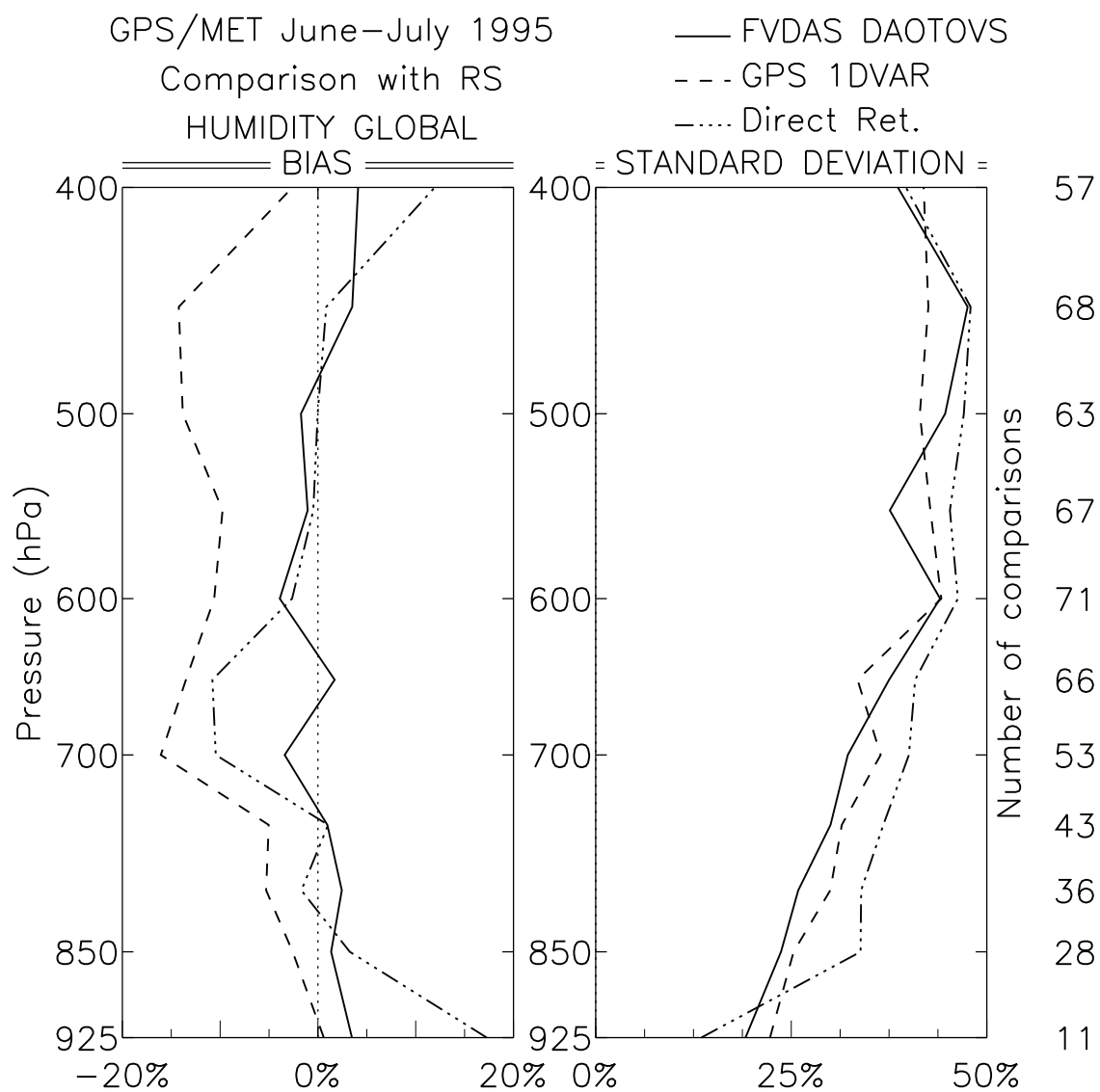
Figure 23: Comparisons with radiosondes humidity, average for the whole domain, without distinction North/Tropics/South. Curves show bias and standard deviation.

Geographic area	North		Tropics	
Sea level pressure (in hPa)	*Mean*	*Std. dev.*	*Mean*	*Std. dev.*
GEOS Assimilation Background (84/31)				
Increment	-1.9	4.0	-4.5	3.7
Background minus RS	0.2	2.7	-0.4	1.2
1DVAR analysis minus RS	-1.7	4.5	-4.9	3.4
FVDAS NESDIS TOVS Forecast Background (102/31)				
Increment	-0.9	4.0	-3.3	3.6
Background minus RS	0.1	2.7	-0.7	1.4
1DVAR analysis minus RS	-0.8	5.0	-4.0	4.1
FVDAS DAOTOVS Forecast Background (91/25)				
Increment	-1.1	4.2	-3.3	3.4
Background minus RS	-0.1	2.7	-0.2	0.9
1DVAR analysis minus RS	-1.2	5.1	-3.5	3.3

Table 3: Sea level pressure statistics for profiles with nearby RS, for the three different backgrounds: GEOS Assimilation and FVDAS NESDIS TOVS (and DAOTOVS) forecasts. The number of cases for each region (North/Tropics) is shown in parentheses.

humidity measurements [*Soden and Lanzante,* 1996]. It is also known that humidity varies over smaller scales than temperature does. In addition, the GPS observations average the refractivity over a long horizontal path whereas RS are somewhat more like point measurements. Clearly, the representativeness problem which arises from the humidity comparison performed here is not properly resolved. We will discuss the humidity results later in section 9.4.

8.4   Sea Level Pressure

The sea level pressure (SLP) is an independent parameter updated by the 1DVAR analysis (see section 7.3). Table 3 shows the mean and standard deviation SLP increment (i.e. 1DVAR analysis minus background).

In the North, the analysis shows a trend to decrease the SLP (negative mean increment) in the three backgrounds. Comparisons with the SLP reported by nearby RS are also shown. The 1DVAR analysis SLP has always both higher bias and standard deviation than the backgrounds, when compared with RS. The bias of the background remains about the same for the three systems (GEOS and FVDAS), whereas the bias of the 1DVAR is significantly reduced when the FVDAS system is used. This suggests that the modifications in SLP created by the 1DVAR do not come only from a misplaced initial background SLP but also from some other phenomena which lead the 1DVAR to believe the SLP is responsible. We will discuss this later in the section that deals with the SLP increments.

In the Tropics, the increments are even greater: -4.5 hPa in the mean with the GEOS Assimilation background, but they are reduced down to -3.3 hPa for the FVDAS DAOTOVS. This latter itself presents both lower bias and standard deviation than

the GEOS Assimilation when compared with RS, testifying once again of the improvement of the system. The same trend is observed for the 1DVAR derived from those backgrounds. Like for the North, the agreement with the SLP reported by RS is always degraded in the analysis as compared with the background.

On the one hand, the SLP increments are needed to fit the background to the observed refractivity. Without these increments, the adjustment occurs in temperature, and the comparisons with the RS are degraded (see section 7.3). But on the other hand, we can see from the Table 3 that these SLP increments do not agree with the SLP reported by RS.

We discuss later in this paper the origin of these SLP increments and the implications for the use of SLP derived from GPS radio occultations into NWP.

9   1DVAR Interpretation of the Refractivity: the Increments

In order to gain some insight in the way the 1DVAR creates increments in temperature, humidity and sea level pressure, we discuss now the refractivity differences between the observations and the background, and how they relate to the analysis increments.

9.1   Innovation and Residual

The innovation is defined here as the difference between the refractivity calculated from the background and the GPS refractivity. The residual is defined as the difference between the 1DVAR refractivity and the GPS. Since refractivity values span several orders of magnitude, we characterize the residual and innovation in terms of percent of observed refractivity. We discuss here the innovation for the three different backgrounds: GEOS Assimilation, FVDAS NESDIS TOVS and FVDAS DAOTOVS.

9.1.1   GEOS Assimilation

Figure 24 shows the mean and standard deviation of the innovation and residual, with the number of points used to build the statistics indicated on the right. All the occultations available after running the 1DVAR, with or without a nearby RS, are used to compute the statistics.

In the North (average of all profiles at latitude above 30°N), the GEOS background refractivity is higher in the mean than the GPS/MET refractivity, except between 7 km and 10 km. The standard deviation of innovation decreases from about 3% around 2 km altitude down to less than 1% between 7 km and 30 km altitude. Below 5 km, the innovation standard deviation grows significantly, indicating contributions from some combination of phenomena that are not simulated correctly by our observation operator, errors in the measurements, errors in the background information
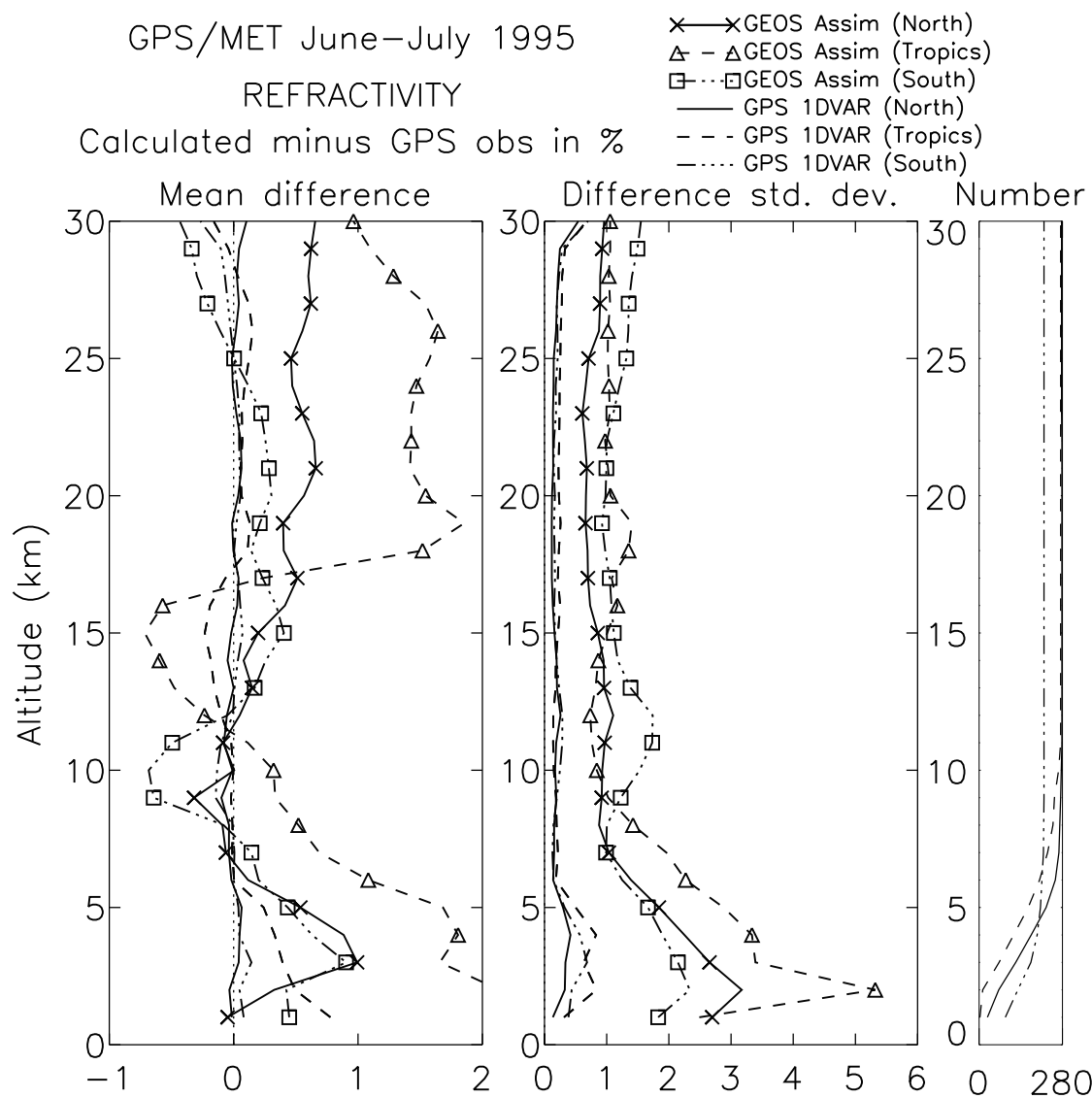
Figure 24: Refractivity calculated from the GEOS background minus observed refractivity, and refractivity calculated from the 1DVAR analysis minus observed refractivity, in percents of the observed refractivity, in the northern hemisphere (solid line), the tropics (dashes), and in the southern hemisphere (dots and dashes).

43

and observation operator.

In the Tropics, we can identify similar features: the mean innovation between 0 and 30 km altitude is positive except between 12 km and 17 km. The standard deviation grows more rapidly than in the North when approaching the surface: 3% at 5 km altitude instead of 2% in the North at the same altitude, maximum of 5.3% at 2 km altitude (note 12 comparisons only for this altitude).

In the South, the innovation bias is similar to the North, i.e. positive up to 8 km altitude and then negative up to 12 km altitude. However, the bias becomes negative again above 25 km altitude. The standard deviations are higher than in North above 8 km altitude. This suggests that the GEOS Assimilation is more accurate at these altitudes in the North than in the South where it is more constrained by RS. Below 8 km, a tentative explanation for the standard deviation being lower in the South than that in the North -even though the forecast is supposed to be more accurate in the North- is perhaps related to the humidity. Since the GPS/MET measurements we are looking at here are for a boreal Summer, the Southern hemisphere undergoes hence winter conditions and the atmosphere is in the mean much drier than in the North, in a specific humidity sense. As seen in section 6.3, this implies that the refractivity is more constrained by the humidity in the North than it is in the South. And since the *temperature* forecasts are better in the North than in the South, this suggests *humidity* as a source of difference.

Other reasons why the innovation standard deviation is higher in the North than in the South include (1) differences in forecast skill, (2) our observation operator which may be unable to simulate properly the refractivity from the humidity features contained in the background. Such shortcomings in the observation operator include 1D vertical integration, horizontal drift of the tangent point not accounted for, no line-averaging effect modeling (spherical symmetry assumption), and violation of geometrical optics assumptions (multipath).

As expected, the 1DVAR has succeeded in pushing the solution refractivity much closer to the GPS/MET observation than the background refractivity. However, in the 1DVAR theory, we assume that both observations and the background are not biased. Clearly they are biased. An interesting point is that even with a bias, the 1DVAR removes some of that bias : the curve for the bias of the 1DVAR refractivity residual is close to zero. However, if we look carefully, some bias remains in the residuals as expected. This is most apparent near the tropopause in the Tropics where the background bias was the strongest. For example, a separate bias correction such as discussed and presented by *Dee and Todling* [2000] is necessary to fully account for these biases.

9.1.2   FVDAS NESDIS TOVS

From Figure 25, we can see that in the North the FVDAS NESDIS TOVS background refractivity bias has about the same shape as the GEOS Assimilation. The negative region has been shifted upwards (8-12 km instead of 7-10 km). Also, the bias curve looks smoother than the GEOS, i.e. less wave structures between 15 km and 25 km altitude. A significant difference resides in the standard deviation shown in Figure 25. It has been decreased by an amount of up to about 1% below 6 km altitude when compared with the GEOS Assimilation. The residuals of the 1DVAR derived from the FVDAS NESDIS TOVS background are similar to those of the 1DVAR derived

from the GEOS Assimilation.

In the Tropics, the whole curve showing innovation bias has apparently been shifted towards more negative values, thus making the average refractivity difference over the whole profile closer to zero and less positive. The standard deviations of the innovation and residual are about the same as with the GEOS background, i.e. slight negative in the residuals around 15 km altitude.

The South presents very similar biases and standard deviations as with the GEOS Assimilation.

9.1.3 FVDAS DAOTOVS

In the North the FVDAS DAOTOVS innovation bias shown in Figure 26 does not present any negative region any more; the crescent-shape of the curve is conserved, though, but with even less waves between 15 km and 25 km altitude, i.e. smoother curve. The innovation standard deviation remains nearly unchanged.

A major difference is observed in the Tropics, where the innovation bias is now confined between -0.5% and 1% above 5 km altitude, whereas before these extrema were -1% and 2% for the FVDAS NESDIS TOVS. This significant reduction of bias, associated with no real change in standard deviation, is another indication of the improvement of the system from NESDIS TOVS to DAOTOVS. It is interesting to notice that a change in the origin of the TOVS data can drastically change the innovation bias curve. This change is not detected in the North, but is much more striking in the Tropics where fewer RS are available to constrain the climatology of the model-analysis.

We observe also a major difference in the South. The innovation bias has been significantly reduced as compared with NESDIS TOVS, but the standard deviation remains identical. This suggests that the performance of the forecast in terms of resolving structures (that we assume in the present discussion to be measured by standard deviation) may have not really changed, but the climatology of the model-analysis, that we can look at using an independent refractivity dataset (GPS/MET), has drastically changed, and has been pulled in the right direction if we assume the GPS/MET observations are non-biased. As in the Tropics, this testifies the TOVS data drive strongly the model-analysis climatology in the Southern hemisphere where only very few RS observations are available.

To summarize, smaller refractivity residuals are observed when the quality of the background is improved. This supports the idea of using GPS refractivity as an independent dataset for model validation studies. In the next three sections we examine and decompose the analysis increments (1DVAR analysis minus background) into sea level pressure, temperature and humidity components to understand how the refractivity differences are minimized in the 1DVAR.
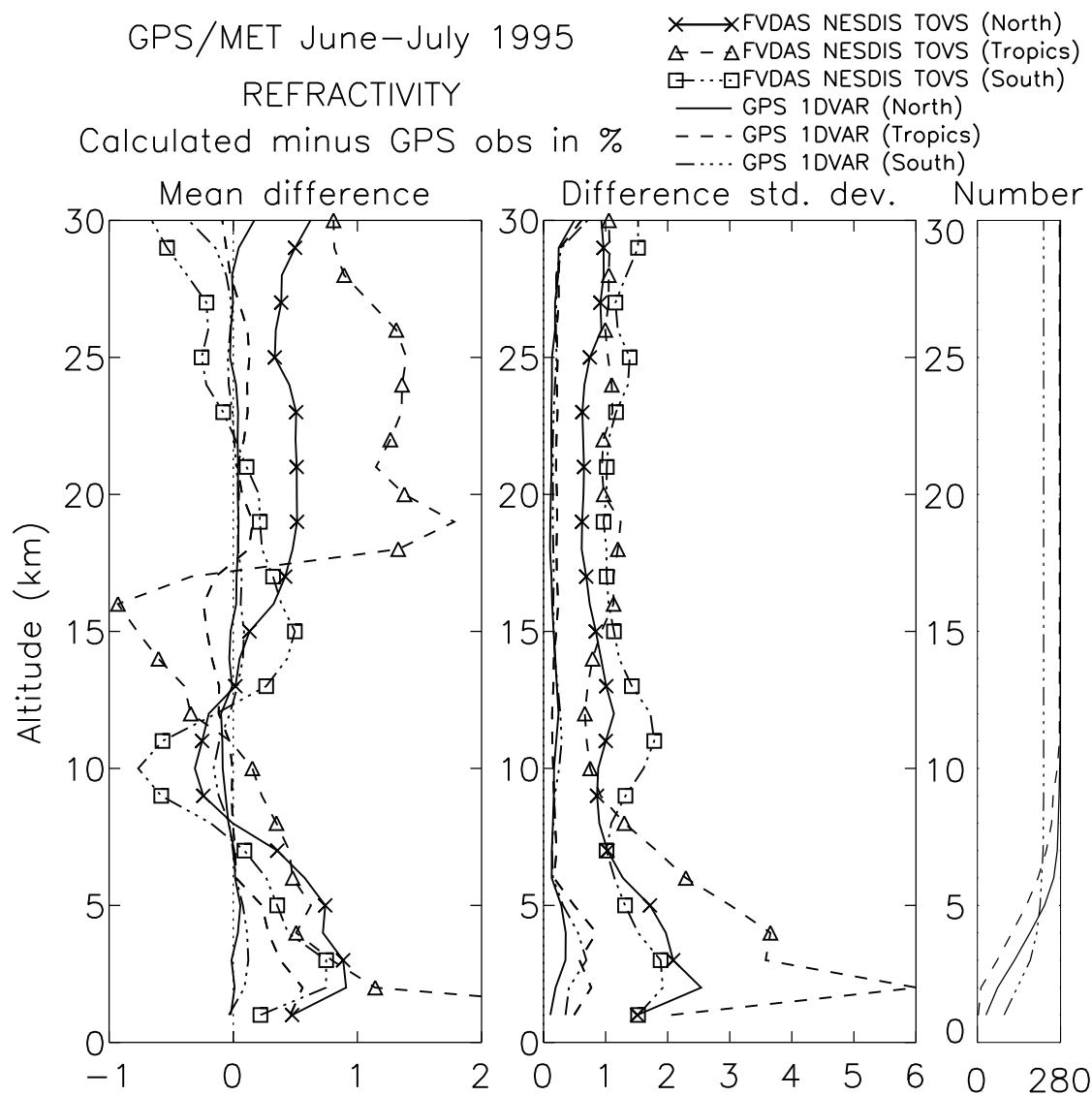
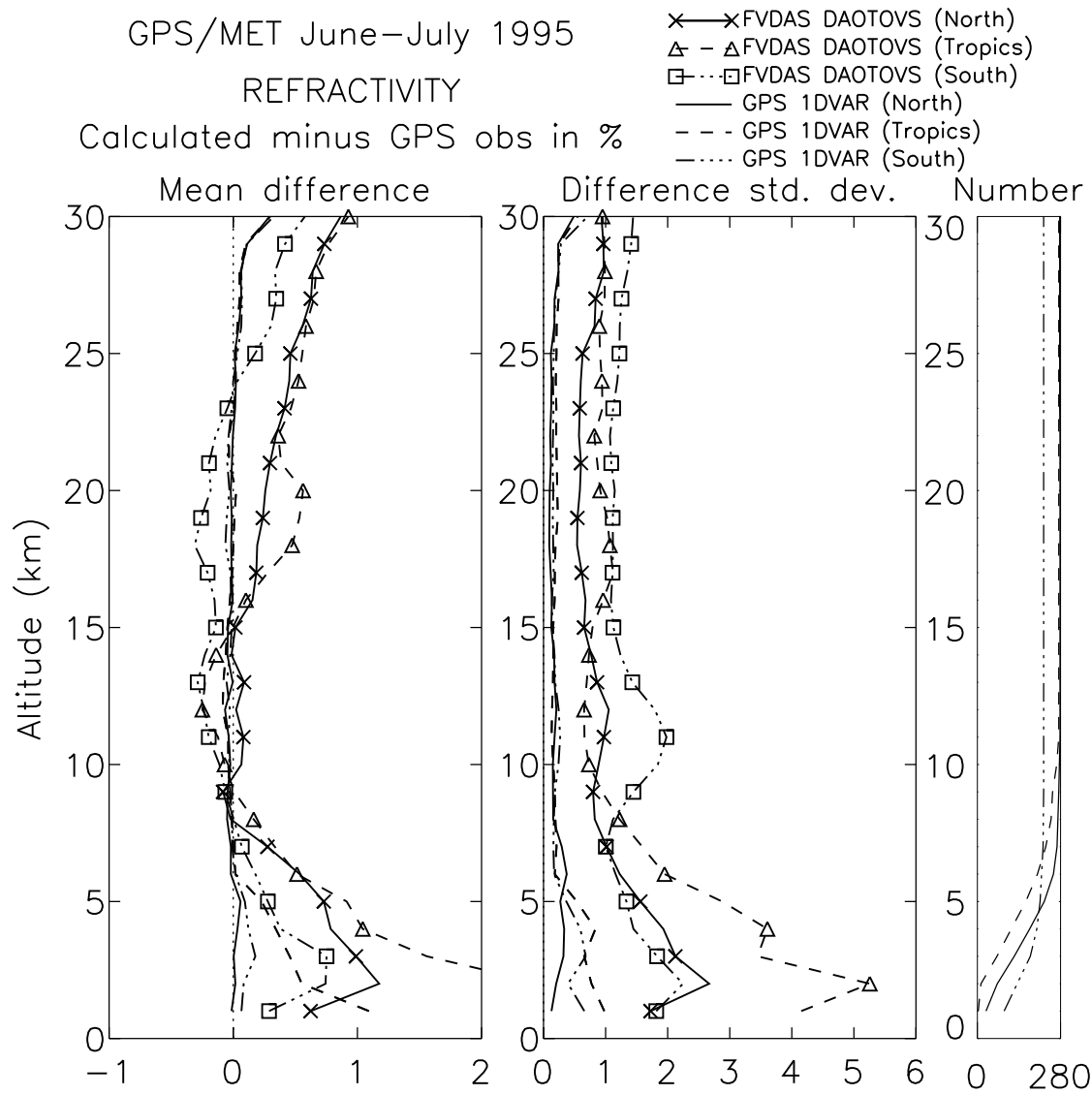Figure 25: Same as figure 24 but for the FVDAS NESDIS TOVS forecast background.

Figure 26: Same as figure 24 but for the FVDAS DAOTOVS forecast background.

9.2 Sea Level Pressure Increments

We begin with the sea level pressure (SLP) since it is the most straightforward to interpret. A SLP shift is somewhat equivalent to a height shift, which itself translates into a fractional refractivity shift: we can approximate the refractivity as varying with a constant scale height H, i.e.

$$N = N_0 \exp^{-\frac{z}{H}} . \tag{14}$$

Then the fractional variation in refractivity at any altitude due to a given height shift Δz is

$$\frac{\Delta N}{N} = -\frac{\Delta z}{H}. \tag{15}$$

From (15) we can predict qualitatively how the 1DVAR analysis modifies the background sea level pressure, given an observed and a background refractivity profile. In the North, Figure 24 shows that the background refractivity is higher in the mean than the observations. This is seen by integrating, on the left hand plot (showing bias), the area Σ_{GEOS} between the zero-mean vertical axis and the innovation curve (GEOS background minus observation). To correct for this positive background minus observation refractivity mean difference in the North, the 1DVAR analysis creates a negative mean SLP increment in this region, which is consistent with the result of Table 3. Likewise, the mean SLP increment is negative in the Tropics, but with a greater SLP mean increment (-4.5 hPa instead of -1.9 hPa in the North) corresponding to a greater area between the zero-mean vertical axis and the innovation curve for this geographical area in Figure 24.

From Figure 25, we compute Σ_{NESDIS} by integrating the area between the residual bias and the zero vertical line. Since not all the occultations reach down to the surface, we integrate between 6 km altitude and 30 km altitude in order to not overweight those few occultations. A similar calculus yields $\Sigma_{DAOTOVS}$ from Figure 26. We find that Σ_{GEOS}=0.33%, Σ_{NESDIS}=0.27% and $\Sigma_{DAOTOVS}$=0.29%. Just keeping in mind the order of those numbers ($\Sigma_{GEOS} > \Sigma_{DAOTOVS} > \Sigma_{NESDIS}$), the SLP increments should then be ranked, from the largest to the smallest: GEOS, FVDAS DAOTOVS, FVDAS NESDIS TOVS. This is confirmed by Table 3, which shows increments in the North of -1.9 hPa, -1.1hPa, -0.9 hPa for GEOS, FVDAS DAOTOVS, and FVDAS NESDIS TOVS, respectively.

Visually, Figure 27 shows the transition, in the North, from the "GEOS" mean curve, representing GEOS residual calculated with the background SLP, to the "1DVAR SLP" mean curve, representing background refractivity calculated with the 1DVAR SLP minus GPS observations. As expected, we can see that the 1DVAR SLP mean curve has been shifted towards more negative values, thus making the integrated area between it and the zero-mean axis now closer to zero. Consequently, the negative refractivity bias observed previously between 7 and 10 km is even more negative. A similar effect can be observed in Figure 28 (Figure 29) for the NESDIS TOVS background (DAOTOVS, respectively).

The three Figures 27, 28 and 29 also show a reduction of standard deviation when going from the residual to the "1DVAR SLP" curve. This suggests that valuable information in terms of height shift between the background and the GPS observations may be contained in the GPS refractivity measurements. It is not completely clear though whether this height shift relates to the first order to an incorrect sea level
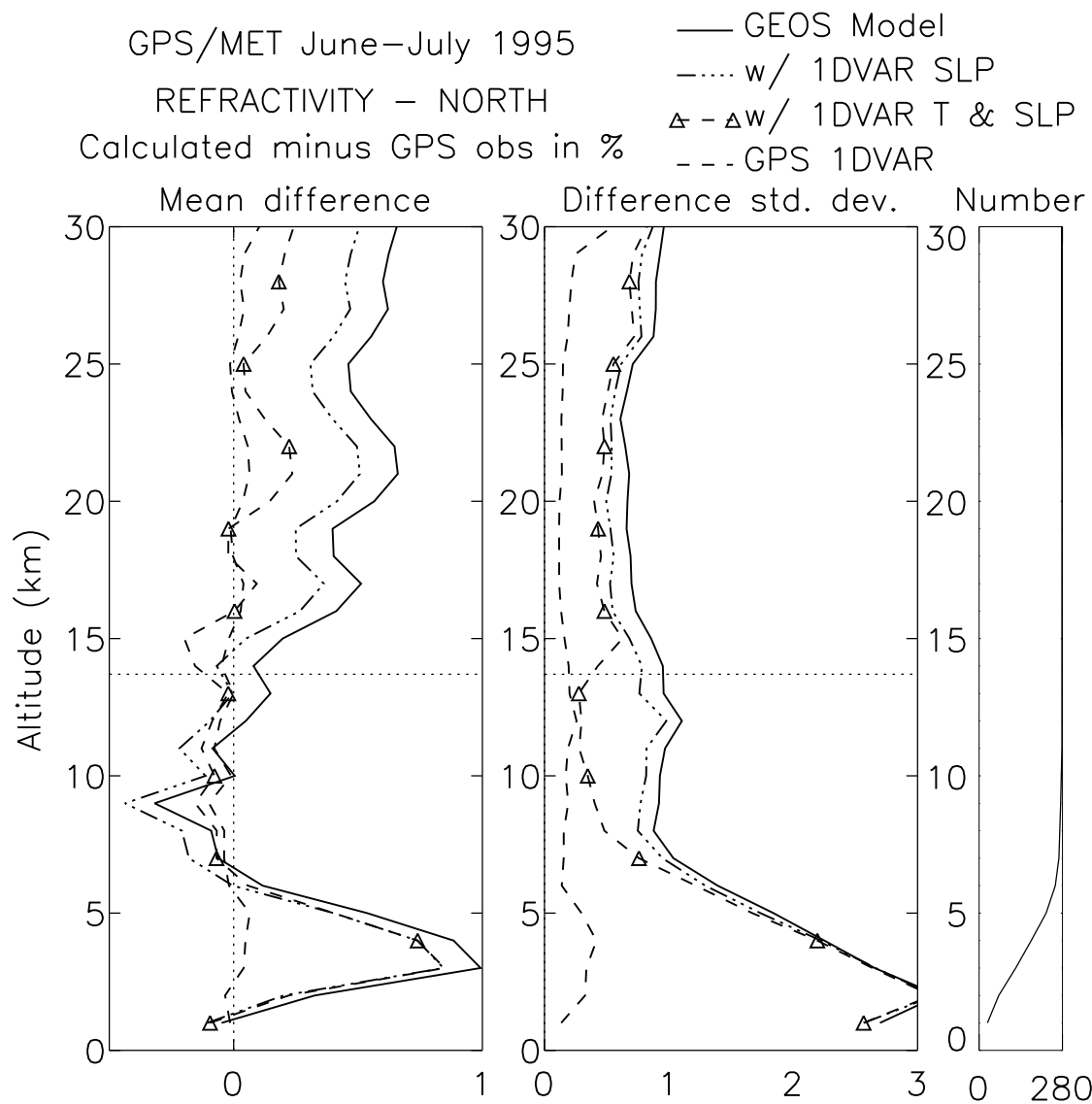
Figure 27: Same as figure 24, North only, using various combinations to generate the calculated refractivity: GEOS background only (solid line), background with 1DVAR SLP (dots and dashes), background with 1DVAR SLP and 1DVAR temperature (triangles) below the 150 hPa level (represented by a horizontal dotted line at 13.7 km altitude), and GPS 1DVAR only (dashes).
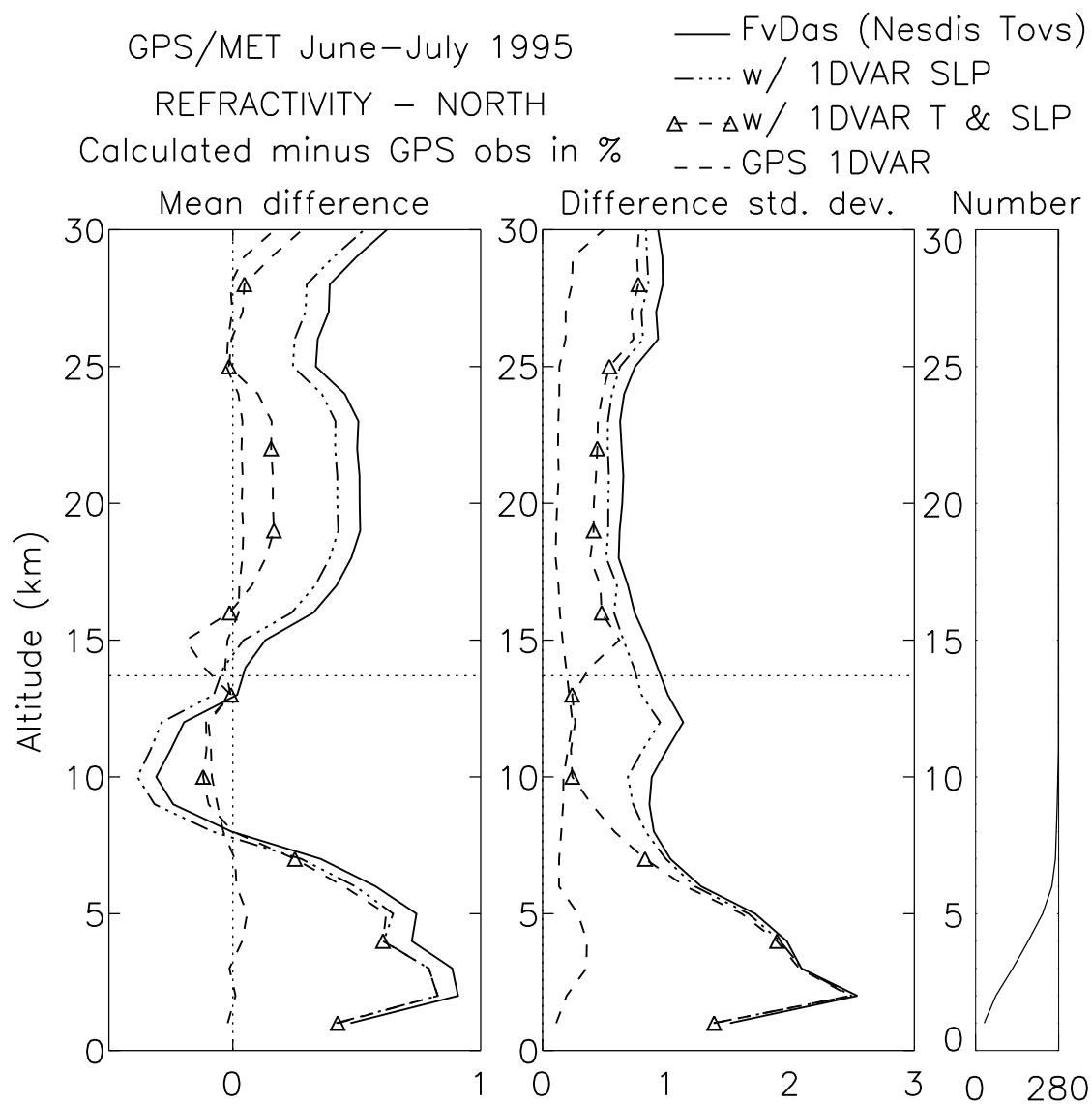
Figure 28: Same as figure 27, but with FVDAS NESDIS TOVS background.
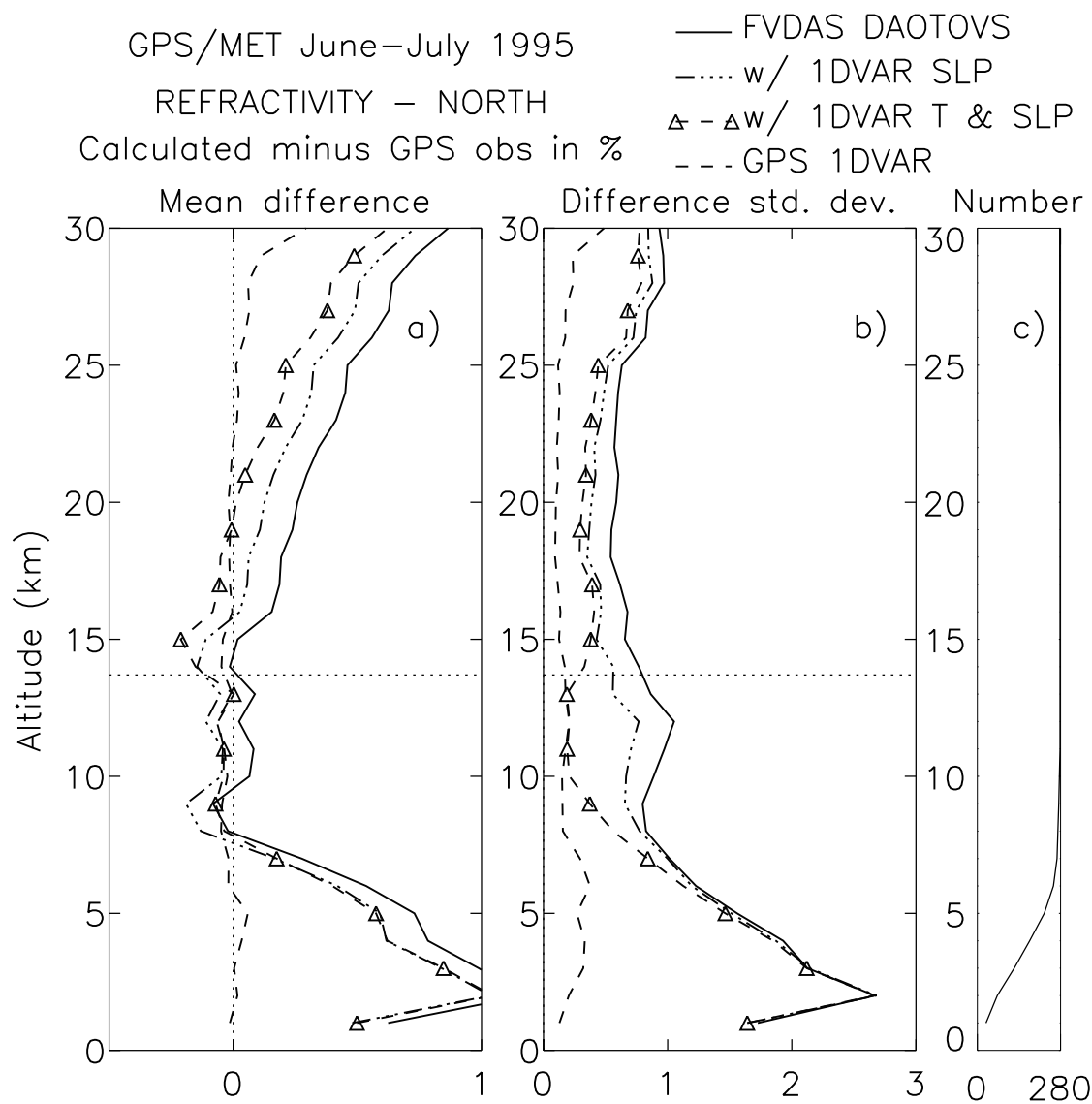
Figure 29: Same as figure 27, but with FVDAS DAOTOVS background.

pressure in the background or if it is primarily due to other sources of error that could be contained either in the measurements or in the observation operator.

It is indeed possible that a discrepancy exists between the references used in the processing of the GPS data and the reference used in the model used as a background (i.e. different geoids). Also, another source of difference might be the spherical symmetry assumption made when deriving the impact parameter (and thus the altitude) of the tangent points from the bending angle measurements. Another track of research could be to investigate the 1D vertical integration performed in the observation operator, that might lead to some systematic bias considering the occultation geometry.

In any case, these discrepancies require further attention before using surface or sea level pressures derived from GPS radio occultation in a weather and/or climate model.

9.3   Temperature Increments

With the SLP already modified, we now examine the temperature increment contribution to the transition from innovation to residual. Temperature has two effects on the refractivity: a local effect (see equation (4)) and a non-local hydrostatic effect (see section 5.6). To separate these two, we now look at the difference between the 1DVAR SLP mean curve and the "1DVAR T & SLP" (noted 1DVAR T_SLP in the rest of the paper) mean curve in Figure 27. The background refractivity in the latter uses 1DVAR SLP and 1DVAR temperature up to the 150 hPa level. So the 1DVAR T_SLP curve includes SLP increments as well as temperature increments up to the altitude of about 13.7 km, represented by an horizontal dotted line in the Figure 27.

Figure 30 represents the temperature increments for the GEOS Assimilation background. They are large near the tropopause. The very tight constraints provided by the relatively small background errors (see Figure 4) limit these increments.

Below 6 km altitude, only small temperature increments are created (Figure 30 below the 500 hPa level), with practically no local influence on the mean refractivity: very little difference appears between the 1DVAR SLP and 1DVAR T_SLP curves in this region. We will discuss the humidity increments in more detail in the next section.

From about 6 to 14 km altitude, we see the local effect of the temperature increments created in the same region; a mean increase in calculated refractivity is related to a mean decrease in temperature (Figure 30, between 500 and 100 hPa) including the 1DVAR correction of the warm bias of the background at the tropopause.

Above about 13.7 km, we should not see any local temperature effect provided the temperature has not changed from the background, but we do see the hydrostatic effect of the negative temperature increments applied below the 150 hPa level; the atmosphere has been shrunk between 6 and 13 km, thus collapsing the whole atmosphere located above. As a consequence, the mean refractivity difference with the observations has been reduced. We note that this hydrostatic adjustment is greater than the modifications due to the SLP change, by comparison between the transition from GEOS to 1DVAR SLP and the transition from 1DVAR SLP to 1DVAR T_SLP mean curves above 14 km. This suggests that the temperature bias at the tropopause might cause the 1DVAR to erroneously change the SLP instead of producing a larger increment in temperature.
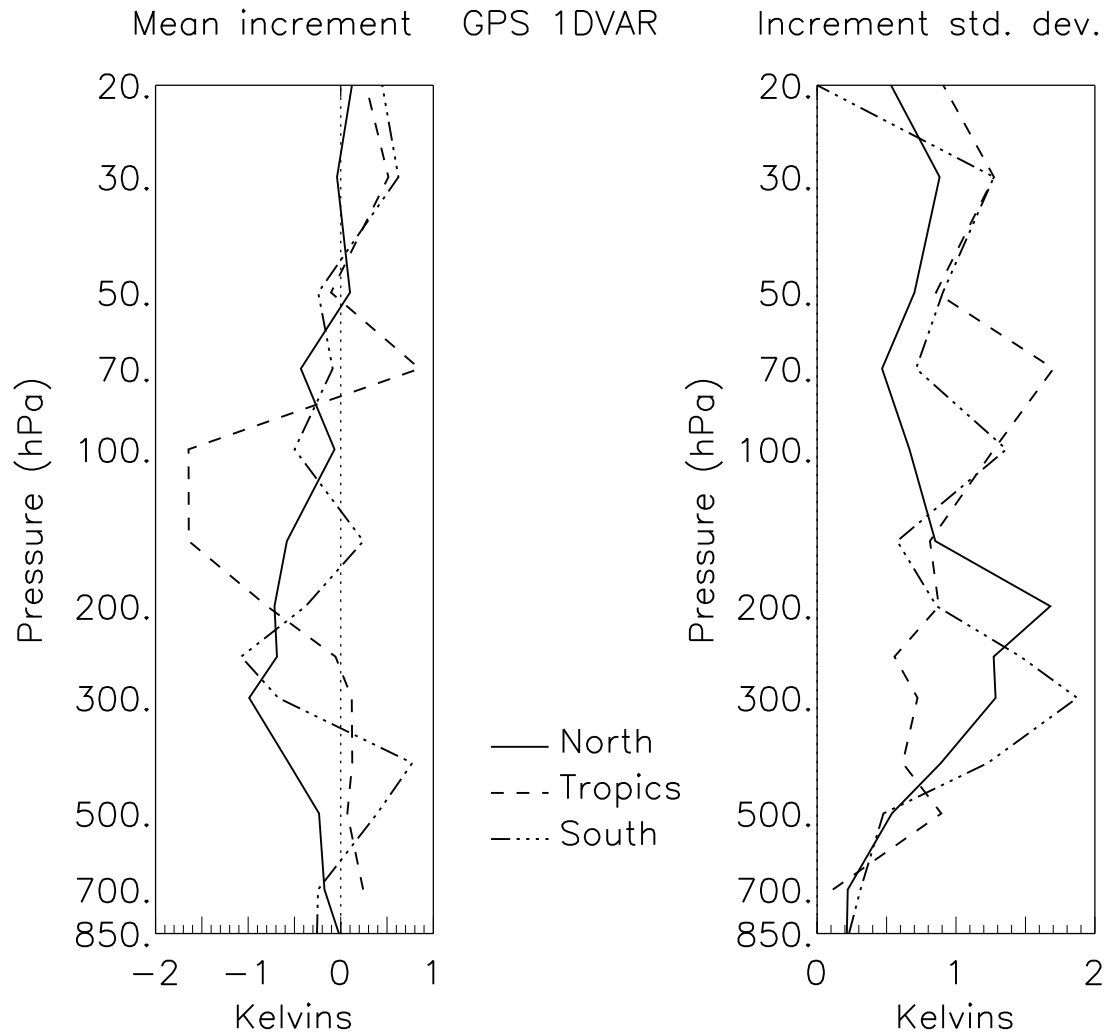
Figure 30: GPS 1DVAR analysis minus GEOS Assimilation background temperature (increments). The number of profiles for each geographic area (North, Tropics, South).

To reduce the remaining positive refractivity difference above 13-14 km altitude, the 1DVAR creates negative temperature increments in the same region (Figure 30) as expected.

A similar discussion can be made for the temperature increments with the FVDAS NESDIS TOVS background shown in Figure 31 (Figure 32). With the FVDAS DAO-TOVS background, the mean temperature increments are less than 0.5 K (1 K) in the North hemisphere (Tropics, respectively), whereas they approach 1 K (2 K, respectively) with the FVDAS NESDIS TOVS background. These two Figures illustrate clearly that the temperature changes induced by the refractivity GPS data depend highly on the other observations already assimilated in the background.

It is worthwhile to note that the mean temperature increments are negative, and that this trend holds for the three backgrounds. This result is consistent with the findings of *Palmer and Barnett,* [2001], who developed an optimal estimation inverse method based on UK Met Office background and GPS/MET bending angles.

9.4 Humidity Increments

With the SLP and the temperature modified, we now examine how the humidity increments contribute to the reduction of the innovation. We are interested in the transition, in Figures 27, 28 and 29, from the 1DVAR T_SLP mean curve to the "GPS 1DVAR" mean curve representing the residual (i.e. 1DVAR minus observation). In terms of bias, the largest differences between these two curves are located between the surface and 7-8 km altitude. The 1DVAR T_SLP mean curve is positive in this region for the three backgrounds, except for the GEOS Assimilation, at 1 km and at 7 km altitudes. Humidity has a local effect on refractivity shown in equation (4). Contrary to temperature, the hydrostatic effect, due to the replacement of dry air by lighter water vapor, can be neglected in the present interpretation (see section 5.6).

In the warm region of the summer North lower troposphere, the refractivity below 8-9 km is primarily dominated by the water vapor. The small temperature increments below 6 km do not reduce significantly the mean innovation in this region. Consequently, the 1DVAR should create negative humidity increments to compensate for the remaining (usually) positive difference in the 1DVAR T_SLP mean curve.

Table 4 shows these increments in percents of the average of background and 1DVAR specific humidity. They agree completely with the postulation of the previous paragraph, i.e. negative humidity increments, except for the GEOS Assimilation at the 850 hPa and 400 hPa levels where the negative innovation imposes a positive humidity increment.

The humidity increment standard deviations are reduced from the GEOS Assimilation to the FVDAS, from 35%-51% down to 18%-34%. This suggests that FVDAS is closer to GPS than GEOS. We found that the FVDAS DAOTOVS humidity is closer to the RS than both GEOS and FVDAS NESDIS TOVS. Then, the reduction of humidity increment standard deviation also validates somehow the FVDAS DAOTOVS humidity.

We now discuss the mixed humidity result obtained by comparison with RS. Considering that the RS and the GPS refractivity represent in essence different averages,

GPS/MET June–July 1995 – TEMPERATURE
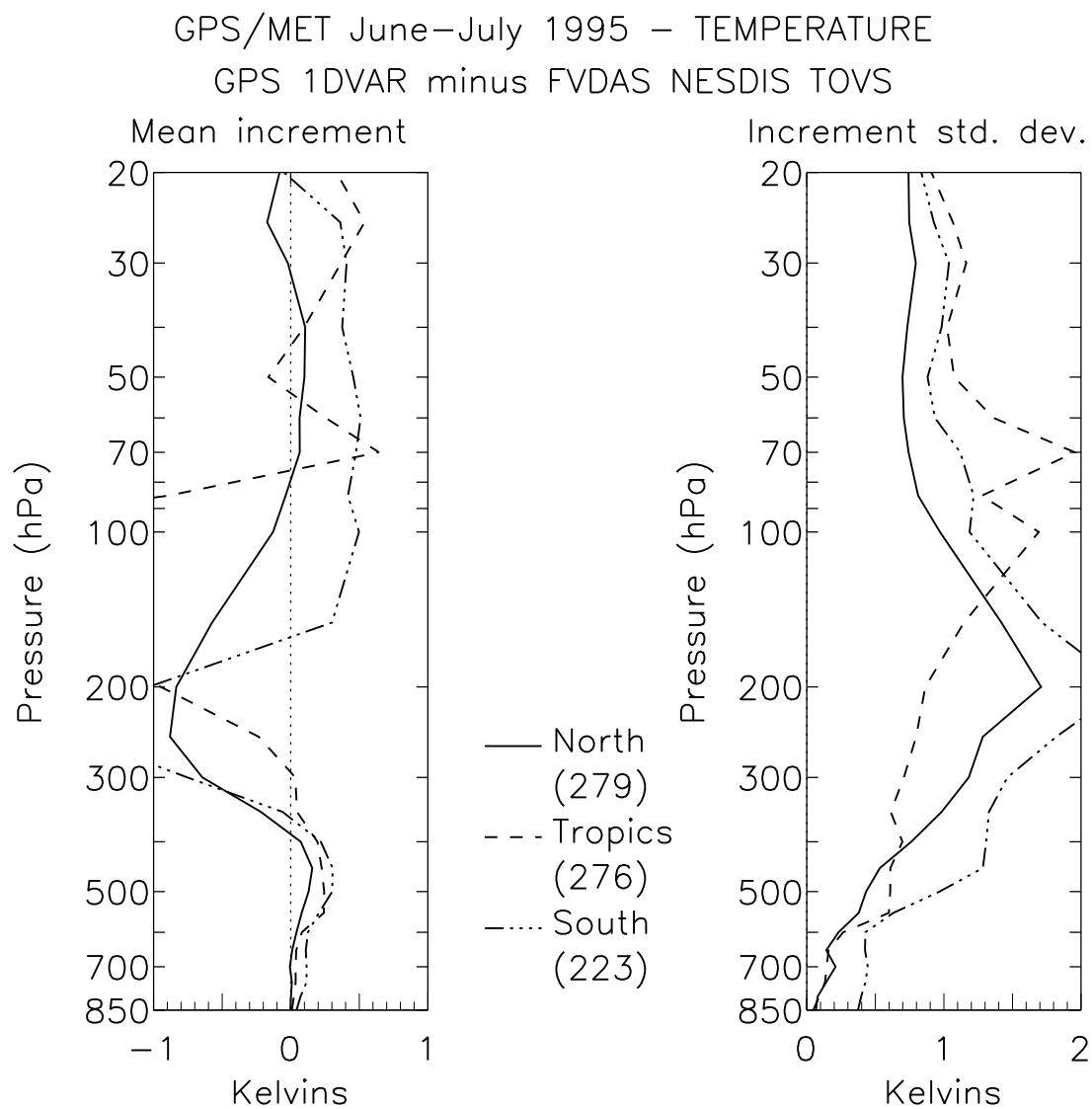GPS 1DVAR minus FVDAS NESDIS TOVS

Figure 31: Same as figure 30 but for the FVDAS NESDIS TOVS background.

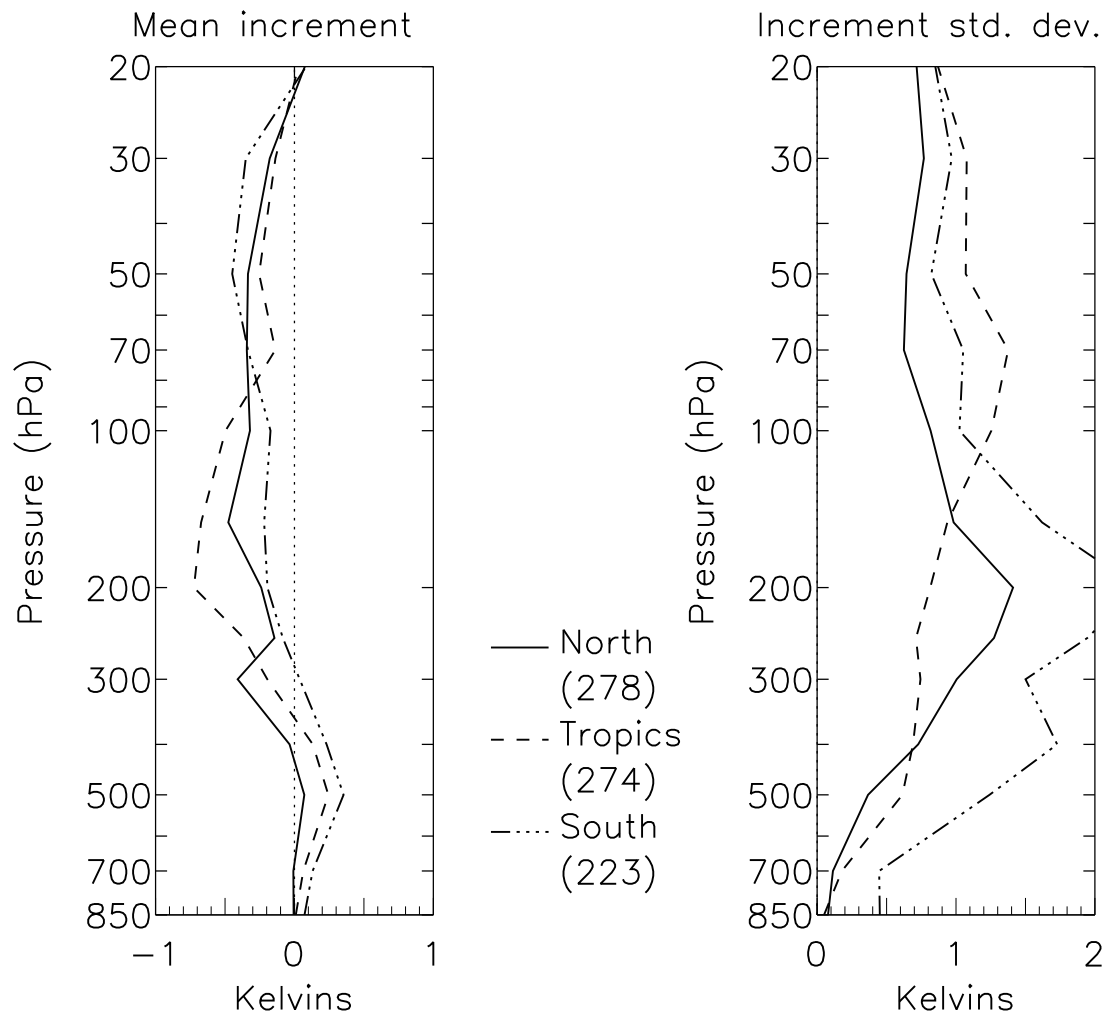GPS/MET June–July 1995 – TEMPERATURE
GPS 1DVAR minus FVDAS DAOTOVS

Figure 32: Same as figure 30 but for the FVDAS DAOTOVS background.

Pressure level	Mean	Std. dev.	Nb. of cases
GEOS Assimilation Background			
850 hPa	2. %	35. %	58
700 hPa	-13. %	40. %	147
600 hPa	-19. %	48. %	221
500 hPa	-7. %	51. %	255
400 hPa	6. %	40. %	271
FVDAS NESDIS TOVS Forecast Background			
850 hPa	-4. %	18. %	60
700 hPa	-12. %	27. %	148
600 hPa	-16. %	31. %	214
500 hPa	-16. %	34. %	239
400 hPa	-7. %	33. %	253
FVDAS DAOTOVS Forecast Background			
850 hPa	-6. %	21. %	61
700 hPa	-11. %	28. %	151
600 hPa	-12. %	32. %	216
500 hPa	-15. %	32. %	239
400 hPa	-8. %	31. %	248

Table 4: Specific humidity increment in the North.

it is somewhat more difficult to demonstrate an impact of the GPS refractivity on the comparison between a humidity retrieved from a line averaged measurement and a point measured humidity. For the temperature, we have seen that this was not a problem, provided we showed that the 1DVAR temperatures were closer to the RS than the background. It is notoriously known that RS humidity is less reliable than temperature. Another possible explanation is the spatial variability of temperature, which is known to be in general less fine than that of humidity. Also, the intrinsic stronger variability of humidity would require a somewhat larger number of comparisons than temperature in order for the comparison to be as much representative as the comparisons involving temperature, whereas here we are in fact confronted with a reversed situation, i.e. a smaller number of available comparisons for the humidity than for the temperature, because of the highly variable quality of the RS humidities. More GPS data are required in order to establish a firm conclusion on the impact of GPS refractivity on the analysis of humidity. However, we have demonstrated that substantial increments are made in the moisture fields after analysis of refractivity, and that small but positive improvements were obtained at some altitudes.

To summarize how the increments are created in the present 1DVAR, we can state that (1) the humidity increments are dominant below 8-9 km (2) the SLP affects all altitudes significantly (3) temperature at and below the tropopause significantly affects the stratospheric residual. In this simplistic scheme, (1) is a local effect, whereas (2) and (3) correspond to a hydrostatic effect.

10 Conclusions and Future Directions

In this paper, we implemented a 1DVAR analysis of refractivity. The approach proved to produce significant adjustments in temperature ($\sim$-0.5 K), humidity($\sim$-10%), and sea level pressure ($\sim$-1 hPa) in the GPS 1DVAR analyses.

We evaluated the potential impact of GPS refractivity data on the analysis of temperature and humidity within the 1DVAR framework *via* simulation studies. The temperature averaging kernels demonstrated that the 1DVAR analysis maintains the relatively high vertical resolution of the GPS observations. Both linear and Monte-Carlo simulations were carried out. They demonstrated the linear approach is valid and representative in the case of the 1DVAR analysis of GPS refractivity. One must include observational error in Monte-Carlo simulations in order to get a representative performance. Not adding observation error to the observations in the Monte-Carlo simulation results in an overestimated impact of the GPS observations. We showed how refractivity constrains differently temperature and humidity depending on the atmospheric conditions (summer or winter). Hence the result of simulation studies depends upon the type of atmospheric conditions. The error covariances estimates also influence the results.

We first applied relatively small background errors (less than 1K in temperature from the surface up to the 5 hPa level) in the simulations. For the observations, we used an error estimate of 0.2% of the observed refractivity above about the 600 hPa level, which is equivalent to the estimate of *Kursinski et al.* [1995,1997], and 2% below. We found that GPS could reduce errors to 0.2-0.5 K from 700 hPa to 2 hPa.

Then, the background errors were increased by a factor of two in general. Based on 1DVAR results with GPS/MET, the refractivity errors were reduced in the lower troposphere to 1% in the Tropics, consistent with *Kursinski et al.* [1995, 1997]. In the Northern and Southern hemispheres, refractivity errors below 5 km altitude were estimated to be 0.4% which is smaller than [*Kursinski et al.,* 1995, 1997]. With summer or tropical conditions, the temperature impact was reduced in the simulations but a much larger impact was obtained in water vapor.

We then applied the 1DVAR analysis method to GPS/MET 1995 data. We showed the importance of performing the analysis with a sufficient number of vertical levels in order to better resolve the structures contained in the GPS refractivity observations. We compared our analyses of temperature with nearby radiosondes (RS). We evaluated the impact of GPS/MET 1995 refractivity data with three sets of backgrounds: GEOS Assimilation (1995), and next-generation FVDAS assimilating either NESDIS TOVS retrievals or interactive TOVS retrievals (DAOTOVS).

As expected from the simulations, we saw a significant improvement in the analyzed temperature as compared with the background (i.e. reduced temperature error bias and standard deviation between 850 hPa and 20 hPa). A warm bias present in the GEOS Assimilation and FVDAS NESDIS TOVS backgrounds at the tropopause was reduced in the analysis, without any specific bias correction. The FVDAS DAOTOVS background proved much closer to the radiosondes (i.e. reduced bias and standard deviation) than the two other backgrounds. As a consequence the 1DVAR obtained using the FVDAS DAOTOVS background presented a significantly reduced bias with respect to the RS. However, the standard deviation was not reduced. This demonstrates that 1DVAR analyses should be performed with the best available background in order to obtain the best retrieval. It is worth noting that the impact induced by

the GPS refractivity data is *relatively* smaller when the background presents a better fit *a priori* with the RS. Generally, the 1DVAR temperatures are colder than the background.

In terms of water vapor, a small number of comparisons ($\sim$70) showed that the 1DVAR humidity difference with the RS presents similar standard deviations as the background. A small improvement in favor of the 1DVAR was observed at the 650 hPa, 500 hPa and 450 hPa levels. The 1DVAR analysis systematically dried the FVDAS DAOTOVS background humidity which presented a very small bias ($\sim$5%) with respect to the RS. As a result, the 1DVAR humidity is too dry when compared with the RS. There are several possible reasons for this result. The sondes are known to have known biases [*Soden and Lanzante*, 1996]. Water structures present small horizontal scales. GPS horizontal resolution (200 to 300 km) is much closer to the background 2$\times$2.5 degrees horizontal resolution than the RS point measurement. Therefore there may be a significant representativeness error.

The background minus observation refractivity innovations present significantly reduced biases and standard deviations with the FVDAS DAOTOVS background than with the GEOS Assimilation. This suggests that GPS refractivity data may be used as an independent benchmark dataset for model validation studies.

We have related the reduction of refractivity innovations in the analysis to the increments created by the 1DVAR. Modifying the sea level pressure in the analysis affects the entire refractivity profiles. Conversely, a global refractivity bias (background minus observation) results in a systematic sea level pressure bias in the 1DVAR analysis. The temperature affects the refractivity profiles in two ways. First, it changes the density inversely, i.e. an increase in temperature causes a decrease in density and refractivity. Second, it has an opposite effect *via* a nonlocal hydrostatic effect: an increase in the analyzed temperature expands the atmosphere, thus increasing the density and refractivity at higher altitudes. The water vapor dominates the refractivity adjustment in the lower troposphere. It has little hydrostatic effect so it is essentially a local effect only.

We have investigated the relationship between the refractivity and sea level pressure. When we used data from GPS/MET we found that the retrieved 1DVAR surface pressures were systematically biased too low as compared with collocated radiosondes reports. The reason for this discrepancy is that GPS refractivities are lower in general than the background. This is also true for ECMWF and UKMO refractivities: such a bias had been seen before in *Kursinski et al.* [1996] and in *Leroy* [1997]. The underlying physical cause of this bias is unclear. We can note that we have two different vertical coordinates: GPS is measured with respect to altitude, whereas model and radiosondes traditionally use the pressure coordinate. The refractivity bias is latitudinally dependent. Clearly this whole issue regarding the refractivity bias needs more attention both for climate and weather applications.

Even though there are assumptions made when deriving refractivity from bending angles (i.e. local spherical symmetry), we showed that in most cases GPS observations combined with a background in an accurate and computationally efficient 1DVAR framework can yield significant improvement in terms of temperature. Mixed but encouraging results were obtained in terms of humidity.

We have used in this study GPS/MET 1995 data, for which the occultations do not extend very low in altitude. We look forward to performing further investigations with new GPS data probing deeper in the troposphere and to carry out data assimilation

experiments when more data are available. Quality control will have to be developed. As an extension to this study, the 1DVAR technique presented here can be improved to account for horizontal drifts and line-of-sight averaging in the observation operator.

Acknowledgments

References

Ahmad, B., and G. L. Tyler, Systematic errors in atmospheric profiles obtained from Abelian inversion of radio occultation data: effects of large-scale horizontal gradients, *Journal of Geophysical Research 104,* 3971-3992, 1999.

Atlas, R., Atmospheric observations and experiments to assess their usefulness in data assimilation, *J. Meteor. Soc. Japan, 75,* 111-130, 1997.

Bean, B. R., and E. J. Dutton, *Radio Meteorology*, 435 pp., Washington, DC, US Govt. Print. Off., 1966.

Bloom, S. C., L. L. Takacs, A. M. da Silva, and D. Ledvina, Data assimilation using incremental analysis updates, *Monthly Weather Review 124,* 1256-1271, 1996.

Cohn, S. E., A. da Silva, J. Guo, M. Sienkiewicz, and D. Lamich, Assessing the effects of data selection with the DAO physical-space statistical analysis system, *Monthly Weather Review 126,* 2913-2926, 1998.

Data Assimilation Office (DAO), Algorithm Theoretical Basis Document (ATBD) version 2, *Draft,* NASA Goddard Space Flight Center, Greenbelt, Maryland, USA, 2000.

Dee, D. P., and A. M. da Silva, Data assimilation in the presence of forecast bias, *Quarterly Journal of the Royal Meteorological Society 124,* 269-295, 1998.

Dee, D. P., and R. Todling, Data assimilation in the presence of forecast bias: the GEOS moisture analysis, *Monthly Weather Review 128,* 3268-3282, 2000.

Eyre, J. R., G. A. Kelly, A. P. McNally, E. Andersson, and A. Persson, Assimilation of TOVS radiance information through one-dimensional variational analysis, *Quarterly Journal of the Royal Meteorological Society 119,* 1427-1463, 1993.

Eyre, J. R., Assimilation of radio occultation measurements into a numerical weather prediction system, *Tech. Memo. 199,* ECMWF, Reading, UK, 1994.

Fjeldbo, G., A. J. Kliore, and V. R. Eshleman, The neutral atmosphere of Venus as studied with the Mariner V radio occultation experiments, *Astron. J., 76,* 123-140, 1971.

Gorbunov, M. E., and S. V. Sokolovskiy, Remote sensing of refractivity from space for global observations of atmospheric parameters, *Rep. 119,* Max Planck-Inst. für Meteorologie, Hamburg, Germany, 1993.

Healy, S. B., A statistical comparison of GPS/MET radio occultation data with numerical weather prediction analyses, *Tech. Rep. 247,* 43 pp., UKMO Forecasting Research, Bracknell, UK, 1998.

Healy, S. B., and J. R. Eyre, Retrieving temperature, water vapour and surface pressure information from refractive index profiles derived by radio occultation: a simulation study, *Quarterly Journal of the Royal Meteorological Society, 126,* 1661-1683, 2000.

Hocke, K., Inversion of GPS meteorology data, *Ann. Geophys., 15,* 443-450, 1997.

Jazwinski, A. H., *Stochastic processes and filtering theory,* 376 pp., Academic Press, New York, USA, 1970.

Jenkins, J. M., P. G. Steffes, D. P. Hinson, J. D. Twicken, and G. L. Tyler, Radio occultation studies of the Venus atmosphere with the Magellan spacecraft .2. results from the October-1991 experiments, *Icarus, 110,* 79-94, 1994.

Joiner, J., and A. M. da Silva, Efficient methods to assimilate remotely-sensed data based on information content, *Quarterly Journal of the Royal Meteorological Society 124,* 1669-1694, 1998.

Joiner, J., and L. Rokke, Variational cloud-clearing with TOVS data, *Quarterly Journal of the Royal Meteorological Society 126,* 725-748, 2000.

Kuo, Y. H., X. Zou, and W. Huang, The impact of global positioning system data on the prediction of an extra-tropical cyclone: an observing system simulation experiment, *Dynam. Atm. and Oceans, 27,* 439-470, 1997.

Kuo, Y. H., S. V. Sokolovskiy, R. A. Anthes, and F. Vandenberghe, Assimilation of GPS radio occultation data for numerical weather prediction, *Terr. Atmos. Ocean. Sci., 11,* 157-186, 2000.

Kursinski, E. R., G. A. Hajj, K. R. Hardy, L. J. Romans, and J. T. Schofield, Observing tropospheric water vapor by radio occultation using the global positioning system, *Geophysical Research Letters 22,* 2365-2368, 1995.

Kursinski, E. R., G. A. Hajj, W. I. Bertiger, S. S. Leroy, T. K. Meehan, L. J. Romans, J. T. Schofield, D. J. McCleese, W. G. Melbourne, C. L. Thornton, T. P. Yunck, J. R. Eyre, and R. N. Nagatani, Initial results of radio occultation observations of Earth's atmosphere using the global positioning system, *Science, 271,* 1107-1110, 1996.

Kursinski, E. R., G. A. Hajj, J. T. Schofield, R. P. Linfield, and K. R. Hardy, Observing Earth's atmosphere with radio occultation measurements using the global positioning system, *Journal of Geophysical Research 102,* 23,429-23,465, 1997.

Kursinski, E. R., G. A. Hajj, S. S. Leroy, and B. Herman, The GPS radio occultation technique, *Terr. Atmos. Ocean. Sci., 11,* 53-114, 2000.

Kursinski, E. R., and G. A. Hajj, A comparison of water vapor derived from GPS occultations and global weather analyses, *Journal of Geophysical Research 106,* 1113-1138, 2000.

Leroy, S. S., Measurement of geopotential heights by GPS radio occultation, *Journal of Geophysical Research 102,* 6971-6986, 1997.

Lin, S. J., A finite-volume integration method for computing pressure gradient force in general vertical coordinates, *Quarterly Journal of the Royal Meteorological Society 123,* 1749-1762, 1997.

Lindal, G. F, H. B. Hotz, D. N. Sweetnam, Z. Shippony, J. P. Brenkle, G. V. Hartsell, and R. T. Spear, Viking radio occultation measurements of the atmosphere and topography of Mars - data acquired during 1 Martian year of tracking, *Journal of Geophysical Research 84,* 8443-8456, 1979.

Lindal, G. F, G. E. Wood, G. S. Levy, J. D. Anderson, D. N. Sweetnam, H. B. Hotz, B. J. Buckles, D. P. Holmes, P. E. Doms, V. R. Eshleman, G. L. Tyler, and T. A. Croft, The atmosphere of Jupiter - an analysis of the Voyager radio occultation measurements, *Journal of Geophysical Research 86,* 8721-8727, 1981.

Lindal, G. F., The atmosphere of Neptune: an analysis of radio occultation data acquired with Voyager 2, *The Astron. J., 103,* 967-982, 1992.

Lindzen, R. S., and M. Fox-Rabinovitz, Consistent vertical and horizontal resolution, *Monthly Weather Review 117,* 2575-2583, 1989.

List, R. J., *Smithsonian meteorological tables,* Smithsonian Institution Press, USA, 1984.

Matsumura, T., J. C. Derber, J. G. Yoe, F. Vandenberghe, and X. Zou, The inclusion of GPS limb sounding into NCEP's global data assimilation system, *Office Note 426,* NOAA/NWS/NCEP, Camp Springs, Maryland, USA, 1999.

Palmer, P. I., Analysis of atmospheric temperature and humidity from radio occultation measurements, D. Phil. thesis, Oxford University, 1998.

Palmer, P. I., J. J. Barnett, J. R. Eyre, and S. B. Healy, A non-linear optimal estimation inverse method for radio occultation measurements of temperature, humidity and surface pressure, *Journal of Geophysical Research 105,* 17,513-17,526, 2000.

Palmer, P. I., and J. J. Barnett, Application of an optimal estimation inverse method to GPS/MET bending angle observations, *Journal of Geophysical Research 106,* 17,147-17,160, 2001.

Pfaendtner, J., S. Bloom, D. Lamich, M. Seablom, M. Sienkiewicz, J. Stobie, and A. da Silva, Documentation of the Goddard Earth Observing System (GEOS) Data Assimilation System - version 1, *Tech. Memo. 104606-4,* NASA, Greenbelt, Maryland, USA, 1995.

Reale, A. L., R. V. Wagener, and T. J. Gardner, TOVS operational sounding upgrades: 1990-1992, *Tech. Rep. 76,* NOAA/NESDIS, Washington, DC, USA, 1994.

Rodgers, C. D., Retrieval of atmospheric temperature and composition from remote measurement of thermal radiation, *Rev. Geophys. and Space Phys., 14,* 609-624, 1976.

Rodgers, C. D., Characterization and error analysis of profiles retrieved from remote sounding measurements, *Journal of Geophysical Research 95,* 5587-5595, 1990.

Schubert, S., C. K. Park, C. Y. Wu, W. Higgins, Y. Kondratyeva, A. Molod, L. L. Takacs, M. Seablom, and R. Rood, A multi-year assimilation with the GEOS-1 system: overview and results, *Tech. Memo. 104606-6,* NASA, Greenbelt, Maryland, USA, 1995.

Soden, B. J., and J. R. Lanzante, An assessment of satellite and radiosonde climatologies of upper tropospheric water vapor, *J. Climate, 9,* 1235-1250, 1996.

Steiner, A. K., G. Kirchengast, and H. P. Ladreiter, Inversion, error analysis and validation of GPS/MET occultation data, *Ann. Geophys., 17,* 122-138, 1999.

Takacs, L. L., A. Molod, and T. Wang, Documentation of the Goddard Earth Observing System (GEOS) General Circulation Model - version 1, *Tech. Memo. 104606-1,* NASA, Greenbelt, Maryland, USA, 1994.

Tyler, G. L., V. R. Eshleman, J. D. Anderson, G. S. Levy, G. F. Lindal, G. E. Wood, and T. A. Croft, Radio science with Voyager-2 at Saturn - atmosphere and ionosphere and the masses of Mimas, Tethys, and Iapetus, *Science, 215,* 553-558, 1982.

Vorob'ev, V. V., and T. G. Krasil'nikova, Estimation of the accuracy of the atmospheric refractive index recovery from Doppler shift measurements at frequencies used in the NAVSTAR system, *Phys. Atmos. Ocean, 29,* 602-609, 1994.

Ware, R. H., M. Exner, D. Feng, M. E. Gorbunov, K. Hardy, B. Herman, Y. H. Kuo, T. Meehan, W. Melbourne, C. Rocken, W. Schreiner, S. Sokolovskiy, F. Solheim, X. Zou, R. A. Anthes, S. Businger, K. Trenberth, GPS sounding of the atmosphere from low earth orbit: preliminary results, *Bulletin of the American Meteorological Society 77,* 19-40, 1996.

Yunck, T. P., G. F. Lindal, and C. H. Liu, The role of GPS in precise Earth observation, paper presented at the Symposium on Position, Location and Navigation, Orlando, Florida, USA, Nov. 29 to Dec. 2 1988.

Zou, X., Y. H. Kuo, and Y. R. Guo, Assimilation of atmospheric radio refractivity using a non-hydrostatic adjoint model, *Monthly Weather Review 123,* 2,229-2,249, 1995.